ON THE MICROPHYSICAL PROPERTIES OF ICE CLOUDS AS INFERRED FROM

THE POLARIZATION OF ELECTROMAGNETIC WAVES

A Thesis

by

BENJAMIN H. COLE

Submitted to the Office of Graduate Studies of
Texas A&M University
in partial fulfillment of the requirements for the degree of

MASTER OF SCIENCE

August 2011

Major Subject: Atmospheric Sciences

On the Microphysical Properties of Ice Clouds as Inferred from the Polarization of

Electromagnetic Waves

ON THE MICROPHYSICAL PROPERTIES OF ICE CLOUDS AS INFERRED FROM

THE POLARIZATION OF ELECTROMAGNETIC WAVES

A Thesis

by

BENJAMIN H. COLE

Submitted to the Office of Graduate Studies of
Texas A&M University
in partial fulfillment of the requirements for the degree of

MASTER OF SCIENCE

Approved by:

Co-Chairs of Committee,	Ping Yang
	Sarah Brooks
Committee Member,	George Kattawar
Head of Department,	Kenneth Bowman

August 2011

Major Subject: Atmospheric Sciences

ABSTRACT

On the Microphysical Properties of Ice Clouds as Inferred from the Polarization of

Electromagnetic Waves.

(August 2011)

Benjamin H. Cole, B.S., University of Dallas

Co-Chairs of Advisory Committee: Dr. Ping Yang
Dr. Sarah Brooks

Uncertainties associated with the microphysical and radiative properties of ice clouds remain an active research area because of the importance these clouds have in atmospheric radiative transfer problems and the energy balance of the Earth. In this study, an adding/doubling model is used to simulate the top of atmosphere (TOA) radiance and full Stokes vector from an ice cloud at the wavelength $\lambda = 865$ nm with many different combinations of assumed ice habits (shapes) and different degrees of ice surface roughness, and the polarized radiance at a wide range of scattering angles is derived. Simulated results are compared with polarized radiance data from the POLDER (POLarization and Directionality of the Earth's Reflectances) instrument on board the PARASOL (Polarization and Anisotropy of Reflectances for Atmospheric Sciences coupled with Observations from a Lidar) satellite.

Bulk ice scattering properties are obtained by using five different size distributions collected during field campaigns ranging in effective diameter from 10 μm

to 90 μm. Bulk scattering properties for the MODIS Collection 5 ice cloud product are used in this study, along with properties for two mid-latitude ice cloud models, a polar/mid-latitude ice model, and a model built for ice clouds over deep convection. Solid columns and hollow columns are used as well.

The polarized radiance simulation results for the moderate surface roughness level best fit the satellite measurements for all ice models, though severely roughened ice crystals do fare well in a few cases. Hollow columns are the best fit to the satellite polarization measurements, but of the ensemble ice models, the polar/mid-latitude model at an effective diameter of 90 μm best fits the polarized radiance measurements for the one day of PARASOL data considered. This model should be the best to simulate ice cloud properties on a global scale.

DEDICATION

To God, to my family, and to my country

ACKNOWLEDGEMENTS

I would like to thank all those in my research group who provided guidance and suggestions for improving my project. I would especially like to thank Yu Xie and Xin Huang for their help.

Many thanks to my committee, especially Dr. Ping Yang. His support and encouragement helped me greatly. Dr. Sarah Brooks provided valuable guidance my first semester as a graduate student at Texas A&M. Dr. George Kattawar provided many helpful suggestions for my research.

TABLE OF CONTENTS

LIST OF FIGURES

LIST OF TABLES

CHAPTER I

INTRODUCTION AND BACKGROUND

Cirrus clouds are very important in the energy balance of the earth, both for
trapping infrared radiation and for reflecting shortwave radiation [1]. They are very high
clouds, generally above 6-7 km, and cover about 30% of the earth's surface at any time,
but can cover up to 60-70% in the tropics where deep convection introduces high-
altitude ice crystals [2]. The magnitude of their surface warming or cooling effect
depends strongly on the cloud height, optical depth, and type and size of ice crystals
present within the cloud [3,4]. Many studies have been done on the microphysical
properties and climatology of cirrus clouds [5-7], but large uncertainties still remain in
the distribution of habits (shapes) and sizes of crystals within cirrus clouds, leading to
potentially inaccurate global climate model (GCM) simulations which include cirrus
clouds [8]. Passive remote sensing observations (remote sensing using solar radiation
instead of a satellite-generated source, such as a laser) of polarized reflectance, coupled
with theoretical modeling of ice cloud properties, have the potential to reduce these
uncertainties since it has been shown that the polarized reflection from an ice cloud is
sensitive to the shape of ice crystals within the cloud [9]. Polarized reflection is also
sensitive to the degree of surface roughness or distortion of the ice crystals [10].

The goals of the current study are outlined in the following five points:

This thesis follows the style of Applied Optics.

- Simulate the upward radiance and Stokes vector from an ice cloud of optical thickness 1 at $\lambda = 0.86$ μm using an adding-doubling radiative transfer model [11] with the assumed ice microphysical properties outlined below, then derive the polarized reflectance to see how sensitive it is to assumed ice microphysical properties.

- Scattering properties for five different combinations of ice habits (shapes) will be generated for use in the model, one for midlatitude/polar regions, two for general ice clouds, one for tropical/deep convection, and one that is used in the MODIS (MODerate resolution Imaging Spectroradiometer) collection 5 ice cloud product. In addition, single habits will also be used.

- Three different levels of surface roughness will be used when deriving scattering properties, smooth, medium roughness, and severe roughness.

- Using measured particle size distributions (PSDs) from field campaigns, ice properties will be developed at five effective diameters from 10 to 90 μm to test the dependence of polarized reflectance on effective diameter.

- All model simulations will be compared to polarized reflectance observed by the POLDER instrument on the PARASOL satellite on August 1st, 2007, to select the ice model which best matches the observations.

Scattering Properties

In order to simulate the reflection of light from a cirrus cloud (cirrus cloud and ice cloud are used interchangeably in this study), the single scattering properties of the ice crystals that make up the assumed cirrus cloud must be calculated. Various field

campaigns have clearly demonstrated that ice crystals found in cirrus are non-spherical and have complicated geometry including aggregates and branched structures, so some way of modeling these complex shapes is needed [12]. There is currently no exact solution for computing the single scattering properties of non-spherical ice crystals for all shapes and sizes [13]. If the geometry can be modeled correctly, several exact methods can be used to obtain the scattering properties for small particles, including the discrete dipole approximation (DDA) and finite difference time domain method (FDTD). For large particles, an approximate method called the improved geometric optics method (IGOM) can be used [14].

Mie scattering theory provides an exact solution for the scattering from a sphere and so is a natural choice for simulations, but spheres are a poor approximation for ice crystals and cannot reproduce many optical phenomena seen in ice clouds, including the $22°$ halo seen in scattering from hexagonal crystals [15]. Geometric ray-tracing calculations can be used for ice crystals which are much larger than the incident wavelength [13], a condition that is usually satisfied with incident solar radiation. Cai and Liou developed the geometric ray-tracing method for non-spherical particles that includes polarization and applied it to the study of randomly oriented hexagonal ice crystals [16]. This technique was improved by Takano and Liou to include more effects such as δ-transmission [15], and Yang and Liou further improved the geometric optics model to give a better treatment of the extinction efficiency [17]. The IGOM model for calculating scattering properties includes all of the previous work and the diffraction effect, which contributes to the forward peak in the phase function. Yang and Liou

compared an FDTD method and the IGOM method and found good agreement for size parameters over 20 μm [17]. Bi et al. [14] detail further improvements to the IGOM model, including a more rigorous mapping of the near-field to the far-field that improves the treatment of forward scattering and removes the δ-transmission term (scattering through two facets of the crystal in the forward direction) completely. Surface roughness has also been included in the updated IGOM model. A perturbation method is used where the normal to the surface is changed for each reflection or refraction event, with three levels of roughness used, smooth (no roughness), moderate roughness, and severe roughness [18]. Surface roughness is explained in more detail in a later section. For this study, the single scattering properties of randomly oriented ice crystals are calculated with the IGOM method.

Based on the observations of the different types of ice crystal habits (shapes) present in the clouds sampled during field campaigns [19], nine different habits were chosen for inclusion in the ice models, including droxtals, plates, solid and hollow bullet rosettes, solid and hollow columns, an aggregate of solid columns, and a small and large aggregate of plates. The scattering properties for these nine habits are computed and used in this study.

Once the single scattering properties are obtained, the bulk scattering properties for a cirrus cloud can be obtained by considering size distributions and habit percentages for each range of sizes in the size distribution. These are based on data from field campaigns, including FIRE-II, ARM, TRMM, MidCiX, Pre-AVE, and others [19]. These data provide over 12,000 particle size distributions (PSDs) for use in constructing

the bulk scattering model, but for this study five size distributions with an effective

diameter (ratio of volume to projected area) between 10 and 90 μm were chosen.

Different percentages of habits for each ice model were used in this study,

including a mixture of percentages developed for polar/mid-latitude ice clouds, one for

deep convective ice clouds, and two general mixtures to fit all ice clouds. These habit

distributions are all potential models for the MODIS collection 6 ice cloud product, and

the current habit percentages from the MODIS collection 5 (C5) ice cloud product model

are used as well. The MODIS C5 ice model is the fifth generation model used in the

retrieval of ice properties on a global scale from the MODIS satellite. This model

assumes six different particle shapes which all have smooth surfaces except the

aggregate of columns, which is severely roughened. The ensemble ice models (models

using many different particle shapes) in this study are models under development for

possible use in the updated collection 6 retrieval algorithms for MODIS. The fractions of

each shape of ice crystal present in each model considered may be found in Appendix A.

Several single-habit bulk scattering models are also used in this study, and different

roughness levels for all the models are considered to determine an appropriate level of

roughness to match PARASOL observations of polarized reflectance.

The spectral response function (SRF) of the satellite sensor to which simulated

data will be compared must also be taken into account along with the solar spectral flux

for the range of wavelengths over which the sensor collects information. Once the bulk

scattering properties are integrated over the SRF and solar spectral flux, they are ready to

be used in the adding-doubling radiative transfer model to produce simulated results for

the top of atmosphere (TOA) Stokes vector from which the polarized reflectance and Mueller matrix may be obtained.

Polarization

Light is a transverse wave composed of electric and magnetic fields, either of which can be used to give a description of the light [20], but the electric field is typically used. If the electric field oscillates in a single plane or if the electric vector describes an ellipse as it propagates through space, the wave is said to be linearly or elliptically polarized. Unpolarized light, on the other hand, is a random mixture of polarization states; no preferential polarization exists. The conventional description of light by Stokes, followed by Chandrasekhar [21], Van de Hulst [22], and others, uses what are now called the Stokes parameters [23]. These are four parameters which completely describe the intensity and state of polarization of a beam of light. The Stokes parameters of different beams can be added if the beams are incoherent, meaning there is no phase relationship existing between any of the beams considered. This is convenient for treating multiple scattering where it is necessary to add the contribution of many different beams into a certain direction.

Chandrasekhar was the first to formally present the radiative transfer equation using the Stokes parameters [24]. The Vector Radiative Transfer Equation, or VRTE, can be used to describe the transfer of polarized radiation through a medium, which will be a cirrus cloud composed of ice crystals in this study. The inclusion of polarization in the radiative transfer problem is necessary for this study since the polarized reflectance from an ice cloud will be modeled and compared with satellite observations.

There have been many methods used to solve the radiative transfer equation. Plass and Kattawar [25] used a Monte Carlo model to study the scattering of light from a water cloud. Using an adding-doubling model which included polarization, reflected and transmitted radiation were calculated by Takano and Liou [15]. In this study, an adding-doubling model [11] will be used to simulate the reflection of light from a cirrus cloud layer, and the full Stokes vector will be obtained, from which the polarized reflectance will be calculated and compared with satellite observations. This model is a plane-parallel model, which assumes that the properties of each layer change only in the vertical. The properties of clouds can change in the horizontal, but for the purposes of this study a plane-parallel model will be sufficient since for non-cumuliform clouds the error arising from the plane-parallel assumption is small [26].

The POLDER Sensor on the PARASOL Satellite

Simulated data from the adding-doubling radiative transfer model will be compared with observations from the POLDER instrument on board the PARASOL satellite. This satellite was launched in December 2004 and became part of the A-Train of satellites, including Aqua, Calipso, Cloudsat, and others [27]. It is a polar-orbiting satellite in a nearly circular sun-synchronous orbit at an altitude of about 705 km and inclination of about 98 degrees [27]. The POLDER instrument is sensitive to linear polarization through the use of a rotating wheel carrying polarizers, and thus, can be used to find the I,Q, and U components of the Stokes vector describing light [28]. It can observe the same pixel at up to 16 viewing directions, and each pixel measures approximately 6x6 km at nadir (looking straight down) [27]. The data used in this study

are from the Level-2 cloud product, which is the Level-1 radiances that have been processed at a larger spatial resolution (about 20x20 km) to derive clouds, thermodynamic phase, different surface types, and other parameters [29]. In this study only pixels that are 100% cloudy, marked as ice, and over ocean are considered in order to minimize polarization effects from land surfaces and water clouds with which the present study is not concerned.

Radiative Transfer

Astrophysicists were the first to make great strides in radiative transfer theory before atmospheric science began to study the problem in detail. Lord Rayleigh in 1871 was the first to study the problem of specifying the radiation field in an atmosphere, and Arthur Schuster and Karl Schwarzschild made important contributions to the understanding of stellar emission lines and radiative equilibrium [21]. Chandrasekhar applied radiative transfer theory to plane-parallel atmospheres and solved the equations describing the phenomenon of the polarization of the sunlit sky that Lord Rayleigh had derived [21]. Reflection and transmission functions can also be used in the radiative transfer problem as an alternative to solving the radiative transfer equation directly [30]. De Haan et al. in their 1986 paper [11] describe a method for calculating the reflection and transmission matrices using the adding-doubling method to study plane-parallel atmospheres. In their model they retrieve the reflection and transmission matrices needed to calculate the scattered radiation for each layer, and then by adding layers together the final solution is built. The adding-doubling model of de Haan et al. will be used to simulate the reflected radiation from an ice cloud in this study.

CHAPTER II

RADIATIVE TRANSFER

The transfer of electromagnetic radiation through a medium can be described using the radiative transfer methodology. After interaction with a medium, radiation contains information about the medium. Reflected solar radiation is chosen as a method to study ice clouds because remote sensing instruments on satellites collect the solar radiation which has interacted with an ice cloud.

Electromagnetic radiation can both travel through a vacuum and through various media, and can be either scattered or absorbed as it interacts with the medium. Scattering redirects the radiation to other directions (sometimes at a different frequency), while absorption transforms the incident radiation into other forms of energy. Scattering and absorption both have the effect of reducing the intensity of the incident beam.

The Radiative Transfer Equation

To get a more detailed picture of the transfer of radiation through a medium, consider a cylinder with length dL and cross sectional area dA, as in Fig. 1. The incident intensity I_λ is attenuated as it goes through the cylinder, becoming I_λ plus dI_λ, the change in intensity due to scattering and absorption. The subscript refers to monochromatic radiation, since the attenuation depends on the wavelength.

The change in intensity of the beam after traversing the medium represented by the cylinder depends on the density of the material ρ, the total distance the beam travels dL, and the mass extinction cross section κ_λ.
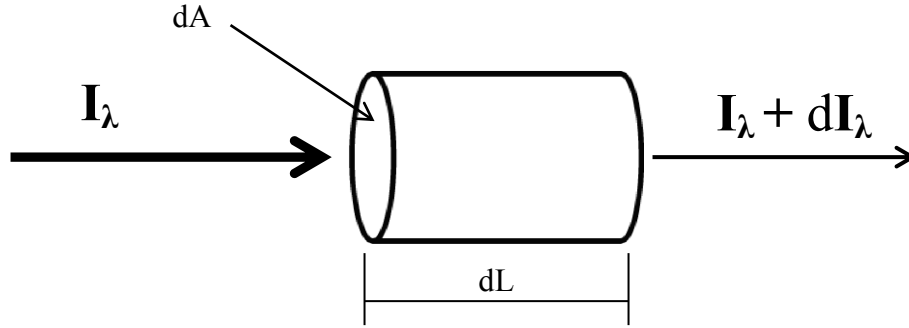
Fig 1. Attenuation in a volume element. Incident radiation, denoted as I_λ, is attenuated by the processes of scattering and absorption upon traversing the medium.

The relationship is given by the following equation:

$$dI_\lambda = -\kappa_\lambda \rho I_\lambda \, dL. \qquad (1)$$

The mass extinction cross section is in units of area/mass and gives the amount of energy removed for both scattering and absorption since it is the sum of the mass extinction and mass scattering cross sections [13].

The perspective given in Fig. 1 is simplified. In radiative transfer a pencil of radiation is considered, where the pencil is confined to a solid angle dω. Fig. 2, adapted from Tynes [31], shows a pencil of radiation at wavelength λ incident upon a volume element of mass dm, cross sectional area dA, and length dL. It scatters into a solid angle dΩ at an angle Θ, called the scattering angle, which is simply the angle between the incoming and outgoing directions. The amount of energy removed from the incident beam due to interaction with the medium in a time t can be expressed as [22]:

$$dE_\lambda = -\kappa_\lambda \rho I_\lambda \cos\theta \, dL \, d\lambda \, dA \, d\omega \, dt. \qquad (2)$$

This includes both scattering and absorption, but they can be analyzed separately.
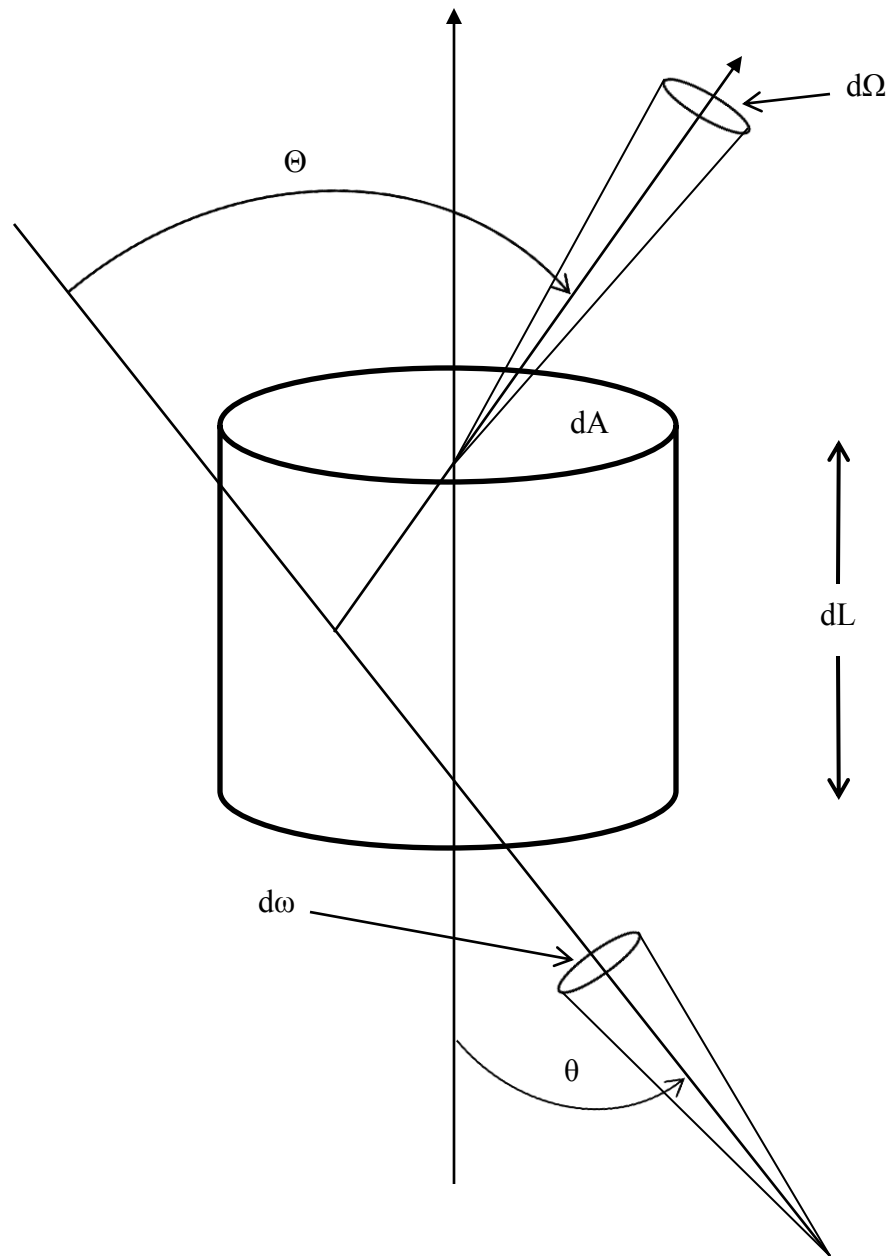
Fig. 2 Radiation incident on a volume element. The mass is given by dm = ρdLdA. It is scattered into the solid angle dΩ through the scattering angle Θ (adapted from Tynes [31]).

Consider first the removal of energy due to scattering. The incident beam may be scattered into any direction, so the phase function P(cosΘ) is introduced to describe the angular distribution of scattered energy. Then the amount of energy scattered into an outgoing solid angle $d\Omega$ (and so removed from the incident beam) is given by:

$$dE_\lambda = -\frac{1}{4\pi} \kappa_\lambda P(\theta, \varphi, \theta', \varphi') d\Theta' \, I_\lambda dm \, d\lambda \, d\omega \, dt \,, \tag{3}$$

where θ' and φ' give the incident direction and θ and φ give the outgoing direction, from which the scattering angle Θ is determined, and dm is defined as $\rho dLdA$. Where only scattering is considered, the phase function is normalized to 1 as follows:

$$\frac{1}{4\pi} \int P(\cos\Theta) d\Omega = 1 \,, \tag{4}$$

but if absorption is considered as well, this becomes an inequality:

$$\frac{1}{4\pi} \int P(\cos\Theta) d\Omega = \widetilde{\omega}_0 \leq 1 \,, \tag{5}$$

where the quantity $\widetilde{\omega}_0$ is called the single scattering albedo. It is the fraction of the total energy removed by scattering, and $1 - \widetilde{\omega}_0$ is the fraction removed by absorption and conversion to other forms of energy.

There are processes in the medium which can contribute to the outgoing energy in a solid angle, including emission by the medium and scattering by the medium from all other directions at the same wavelength into the solid angle considered. The amount of energy gained in that interval $d\omega$ is:

$$dE_\lambda = j_\lambda \, dm \, d\lambda \, d\omega \, dt \,, \tag{6}$$

where j_λ is the emission coefficient describing the rate at which the medium emits energy.

If the single scattering albedo is greater than zero, scattered radiation from all other directions has to be taken into account for the intensity in the outgoing solid angle of interest. Using equation 3 for the contribution of this scattered radiation, we can set it equal to equation 6 and then solve for j_λ:

$$j_\lambda = \frac{\kappa_{s\lambda}}{4\pi} \int_0^{2\pi} \int_0^{\pi} P(\theta, \varphi, \theta', \varphi') I_\lambda(\theta', \varphi') \sin\theta' d\theta' d\varphi' . \qquad (7)$$

The mass extinction cross section now takes on an extra s subscript, indicating this is the contribution into the final solid angle from scattering only.

The contribution to the outgoing energy from material emission comes from thermal emission of the medium, which is assumed to be in local thermodynamic equilibrium (LTE). The material acts like a blackbody and behaves according to the Planck distribution, but the emission from this source can be neglected since it is so small in comparison to the radiation received by the sun [13]. This study uses reflected solar radiation, meaning thermal emission will not be considered here.

Now we have all the parts in place to calculate the total change in energy of an incident beam that interacts with a medium from extinction of the incoming beam and scattering into the outgoing beam from all other directions. Consider again a setup as in Fig. 1, where a beam of radiation is normally incident ($\cos\theta = 1$) on a cylinder and goes through its length dL. The amount of energy removed is given by Eq. (2), and the amount of energy added is given by Eq. (6), and adding them we arrive at the total:

$$dE_\lambda = -\kappa_\lambda I_\lambda \rho \, dL \, d\lambda \, dA \, d\omega \, dt + j_\lambda \, \rho \, dL \, d\lambda \, dA \, d\omega \, dt . \qquad (8)$$

Then, because the energy difference can be written in the following way,

$$dE_\lambda = \frac{dI_\lambda}{dL} \, dL \, d\lambda \, dA \, d\omega \, dt \,, \tag{9}$$

the radiative transfer equation can finally be written as the following:

$$\frac{dI_\lambda}{\kappa_\lambda \rho dL} = -I_\lambda + J_\lambda \,. \tag{10}$$

The source function J_λ is given by:

$$J_\lambda = \frac{j_\lambda}{\kappa_\lambda} \,. \tag{11}$$

The radiative transfer equation here is the one defined by Chandrasekhar [21]. On the

right hand side of Eq. (10), the first term is the contribution to the outgoing radiation in

the direction (θ, φ) from extinction of the incident beam (so actually a subtraction) and

the second term is a source term describing the addition of energy from scattering into

the outgoing direction (θ, φ) from all other directions.

Both direct and diffuse intensity contribute to the outgoing radiation in the

problem of radiative transfer, but remote sensing using reflected solar radiation

(neglecting thermal emission) deals only with diffuse intensity, included in the source

function J. In addition, the subscript λ can be left out as long as the reader is aware that

the equations are defined for a wavelength interval λ to $(\lambda + d\lambda)$. Thus far, the radiative

transfer equation has been developed in scalar form only. The vector radiative transfer

equation, including polarization, will be introduced in a later chapter.

Equation of Radiative Transfer for Plane-parallel Atmospheres

Following Liou [13], we will now define the radiative transfer equation for a

plane-parallel atmosphere, which means that any parameters in the model change only in

the vertical. This simplified model of the atmosphere is used in the adding-doubling

code of de Haan [11] to solve for the upward intensity and will be utilized in the present

study.

Distance is measured normal to the plane in which parameters are invariant

horizontally, and is generally taken to be the +z direction. Fig. 3, adapted from Liou

[13], gives an overview of the geometry associated with the plane-parallel model.

Distances in the horizontal are infinite, while distances in the vertical are finite.

Referring to Fig. 3, the distance traveled in the vertical direction z along a

position vector **s** is simply:

$$dz = \cos\theta \, ds \, . \tag{12}$$

The azimuth angle φ is measured from a plane containing the z-axis and the x-axis. In

the adding-doubling model used in this study, the relative azimuth angle is considered,

which is simply the difference between the azimuth angle of the incoming direction and

the outgoing direction, $\varphi - \varphi'$. The zenith angle θ is measured from the +z direction.

Now we can write the radiative transfer equation in terms of plane-parallel geometry as:

$$\cos\theta \frac{dI(z,\theta,\varphi)}{\kappa\rho dz} = -I(z, \theta, \varphi) + J(z, \theta, \varphi) \, . \tag{13}$$

A direction cosine $\mu = \cos\theta$ can be defined, along with the optical thickness τ:

$$\tau = \int_z^\infty \kappa\rho \, dz \, . \tag{14}$$
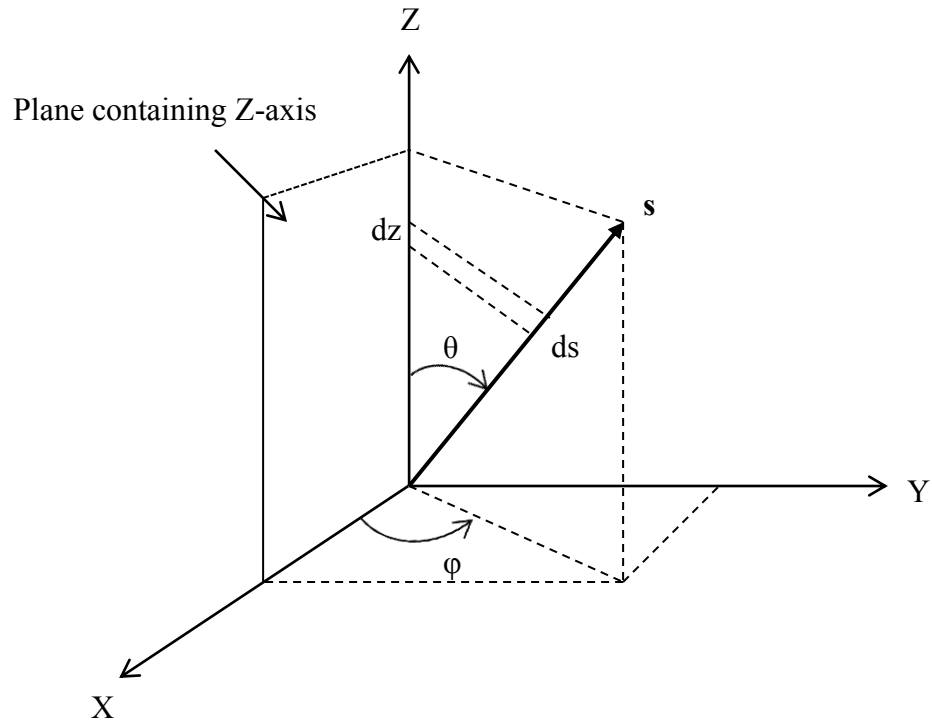
Fig 3. Geometry for a plane-parallel atmosphere. φ is the azimuth angle measured with respect to a plane containing the Z-axis, θ is the zenith angle with respect to the +Z direction, and s is the propagation direction. The component of s along z is given by s*cosθ.

The optical thickness is measured downward from the outer boundary. Using these two definitions the radiative transfer equation can be written as the following:

$$\mu \frac{dI(\tau,\mu,\varphi)}{d\tau} = I(\tau, \mu, \varphi) - J(\tau, \mu, \varphi) \ . \tag{15}$$

This is the same equation given in Liou [13] and is the basic equation that must be solved to treat the problem of multiple scattering in plane-parallel atmospheres.

CHAPTER III

POLARIZATION AND THE

VECTOR RADIATIVE TRANSFER EQUATION

The Electric Field as a Vector

Thus far, the radiative transfer equation has been considered in a scalar form only. We need the vector form of the equation if we want to consider phenomena such as polarization in solar passive remote sensing, because light is a vector quantity and the direction of its electric field determines the polarization. Adams and Kattawar [32] also showed that there was an error introduced in the radiance measurements if polarization is not considered since the intensity is not completely independent of the state of polarization.

Electromagnetic radiation is a transverse wave, which means that the oscillations of its electric and magnetic fields occur perpendicular to the direction of propagation, as Maxwell showed in the 1800s [20]. Either the electric or magnetic field may be used to specify the polarization state of the electromagnetic wave, but historical convention will be followed and the electric field will be used to define the polarization direction.

As a vector, an electromagnetic wave can be described as the sum of two components. If we define a meridian plane as a plane containing the direction of propagation and the zenith direction (+z direction in this case), then the electric field can be written as the sum of a component parallel with this meridian plane and a component perpendicular to the meridian plane. Both components are perpendicular to the

propagation direction. See Fig. 4, similar to Fig. 3, for the geometry involved. The

equation for this plane wave is:

$$\vec{E} = \vec{E}_{\parallel} + \vec{E}_{\perp} = \left[E_{\parallel}\hat{\theta} + E_{\perp}\hat{\varphi}\right]\exp\{-i(k\hat{n}\cdot\vec{r} - \omega t)\}. \qquad (16)$$

The direction of propagation is $\hat{n}$, which is in the meridian plane, defined earlier and

seen in Fig. 4. The vector $\vec{r}$ connects the origin to the observation point, ω is the angular

frequency, k is the wavenumber, and the unit vectors $\hat{\theta}$ and $\hat{\varphi}$ are perpendicular to the

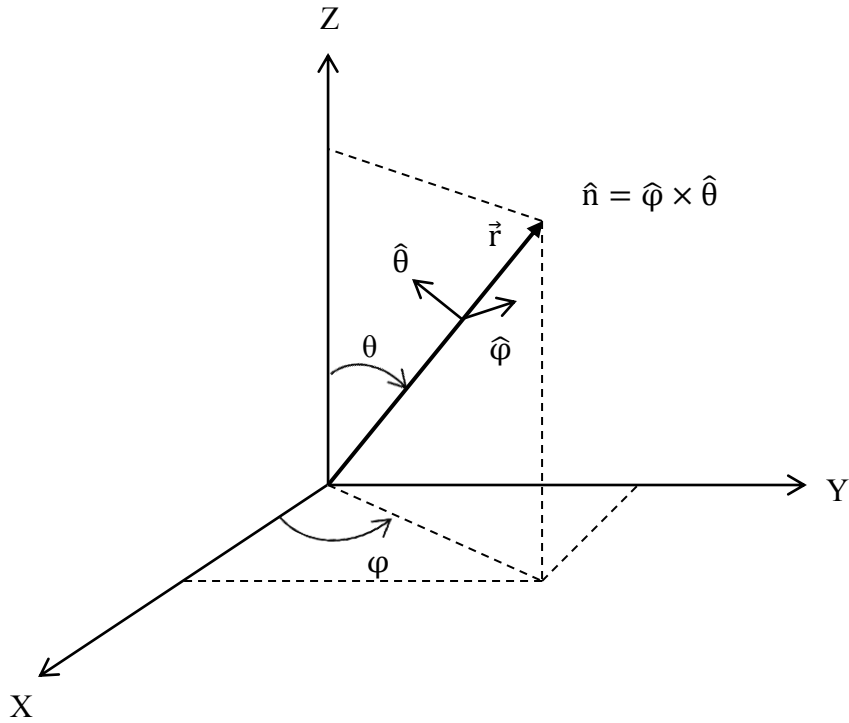propagation direction, so that $\hat{\varphi} \times \hat{\theta} = \hat{n}$.

Fig. 4. Coordinate system for the electric field. The meridian plane is in the $\hat{\theta}$ direction.

$E_\parallel$ and $E_\perp$ are actually complex amplitudes with an amplitude and phase, so the previous

equation can be written:

$$\vec{E} = \left[a_\parallel \exp(-i\delta_\parallel)\,\hat{\theta} + a_\perp \exp(-i\delta_\perp)\,\hat{\varphi}\right]\exp\{-i(k\hat{n}\cdot\vec{r} - \omega t)\}. \qquad (17)$$

Chandrasekhar [21] pointed out that for unpolarized electromagnetic radiation, the

complex amplitudes are not static in time and space, and indeed must not be a function

of each other. If relationships exist among these components, the beam can be said to be

polarized in some way.

Polarization

The most general form of polarization is elliptical, where the tip of the electric

field vector traces out an ellipse when an observer views along a beam traveling toward

him, as in Fig. 5. Linear and circular polarization are special cases of elliptical

polarization for certain conditions on the amplitude and phase difference

$\delta = \delta_\parallel - \delta_\perp$ of the components. See Table 1 for a compilation of the possible

polarization states. The total electric field for each case can be obtained simply by

inserting the values from Table 1 into Eq. (17).

Table 1. Polarization states. The associated amplitude and phase difference components
are also shown (adapted from Lawless [33]).

State of polarization	Amplitude relationship	Phase difference $\delta = \delta_\parallel - \delta_\perp$
Elliptical	$a_\parallel \neq a_\perp$	$\neq 0$ $\neq \pm 2m\pi \qquad m = 1,\infty$
Linear	$a_\parallel \neq a_\perp$ or $\quad a_\parallel = a_\perp$	$= 0$ $= \pm 2m\pi \qquad m = 1,\infty$
Circular	$a_\parallel = a_\perp$	$= \pm(2m+1)\frac{\pi}{2} \quad m = 0,\infty$
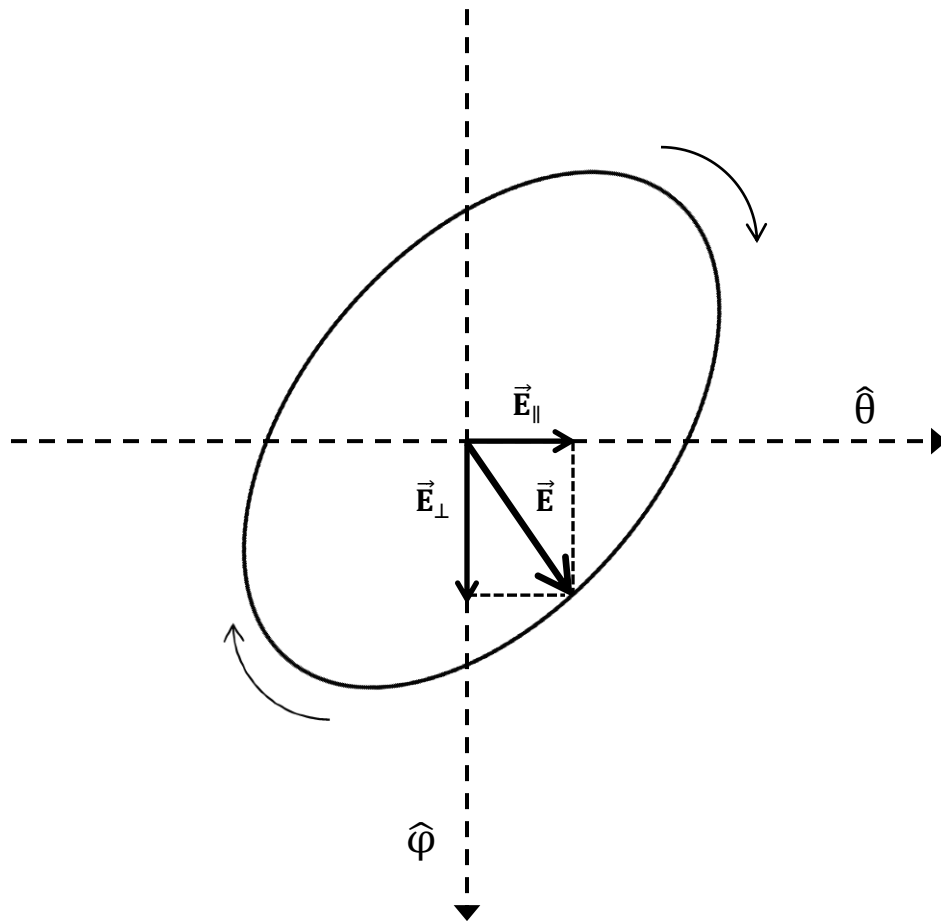
Fig. 5. Elliptically polarized beam. The propagation direction is out of the page and the electric field vector traces out an ellipse in the clockwise direction through time.

According to Hecht [34], natural light (solar radiation) is unpolarized, composed of rapid fluctuations in polarization state that make it impossible to discern any preferred polarization. In effect, the polarization ellipse of the beam of radiation rapidly changes shape and orientation in time. A better name, then, would be randomly polarized radiation instead of unpolarized radiation. This study will be concerned with randomly

polarized radiation from the sun. In order to begin to incorporate the concept of polarization into the radiative transfer equation, a method for mathematically representing the polarization state of a beam of radiation in the equation must be introduced. Chandrasekhar [21] adopted the Stokes parameters, derived in 1852 by Sir George Stokes [23], for this purpose in his treatment of polarization in the radiative transfer equation.

The Stokes Parameters

Chandrasekhar realized that to completely describe a radiation field, the intensity, plane and degree of polarization, and ellipticity need to be specified. It would be very difficult, as he says, to include "an intensity, a ratio, an angle, and a pure number in any symmetrical way in formulating the equations of transfer" [21]. The Stokes parameters can represent all four of these quantities, and can be included in the radiative transfer equation in the place of the scalar intensity I.

The Stokes vector is a four-element column vector composed of I, Q, U, and V, the four Stokes parameters. These are measurable quantities, where I is the intensity, Q represents the linear polarization either parallel or perpendicular to some axis, U represents the linear polarization at $+45°$ or $-45°$ to that axis, and V represents the circular polarization. There are many equivalent ways to define them mathematically, and three ways will be presented here.

Following van de Hulst [22], the Stokes parameters can be written in the following form (c.f. Eq. (16)):

$$I = E_\parallel E_\parallel^* + E_\perp E_\perp^*$$

$$Q = E_\parallel E_\parallel^* - E_\perp E_\perp^*$$

$$U = E_\parallel E_\perp^* + E_\perp E_\parallel^*$$

$$V = i(E_\parallel E_\perp^* - E_\perp E_\parallel^*) \,, \tag{18}$$

where the asterisk denotes a complex conjugate. A constant term $(k/2\omega\mu_0)$ [35] has been omitted from each of the Stokes parameters because in most cases the relative Stokes parameters are examined, not the absolute Stokes vector. The constant is important to remember because it gives the Stokes vector components the units of energy per area per time, or irradiance.

Alternatively, considering the plane wave equation for the electric field with amplitude a and phase δ for each component (c.f. Eq. (17)), the Stokes parameters can be written as follows:

$$I = a_\parallel^2 + a_\perp^2$$

$$Q = a_\parallel^2 - a_\perp^2$$

$$U = 2a_\parallel a_\perp \cos \delta$$

$$V = 2a_\parallel a_\perp \sin \delta \,. \tag{19}$$

Again, the δ here is the phase difference $\delta_\parallel - \delta_\perp$ of the components.

However, there is a third way to represent the Stokes parameters, perhaps more intuitive than the first two ways.

If we construct a polarization ellipse as in Fig. 6, then the electric field vector may be written as follows:

$$\vec{E} = a\hat{p}\cos\beta\sin(\omega t - k\hat{n}\cdot\vec{r} + \alpha) + a\hat{q}\sin\beta\cos(\omega t - k\hat{n}\cdot\vec{r} + \alpha) \ . \quad (20)$$

The unit vectors $\hat{p}$ and $\hat{q}$ are unit vectors along the long and short axes, respectively, and α is an arbitrary phase angle. The Stokes parameters may then be recast in the following form:

$$I = a^2$$

$$Q = a^2\cos 2\beta\cos 2\chi$$

$$U = a^2\cos 2\beta\sin 2\chi$$

$$V = a^2\sin 2\beta \ . \quad (21)$$

The quantity $\tan\beta$ gives the ellipticity, and is 0 for linear polarization, -1 for left-circular polarization, and +1 for right-circular polarization.
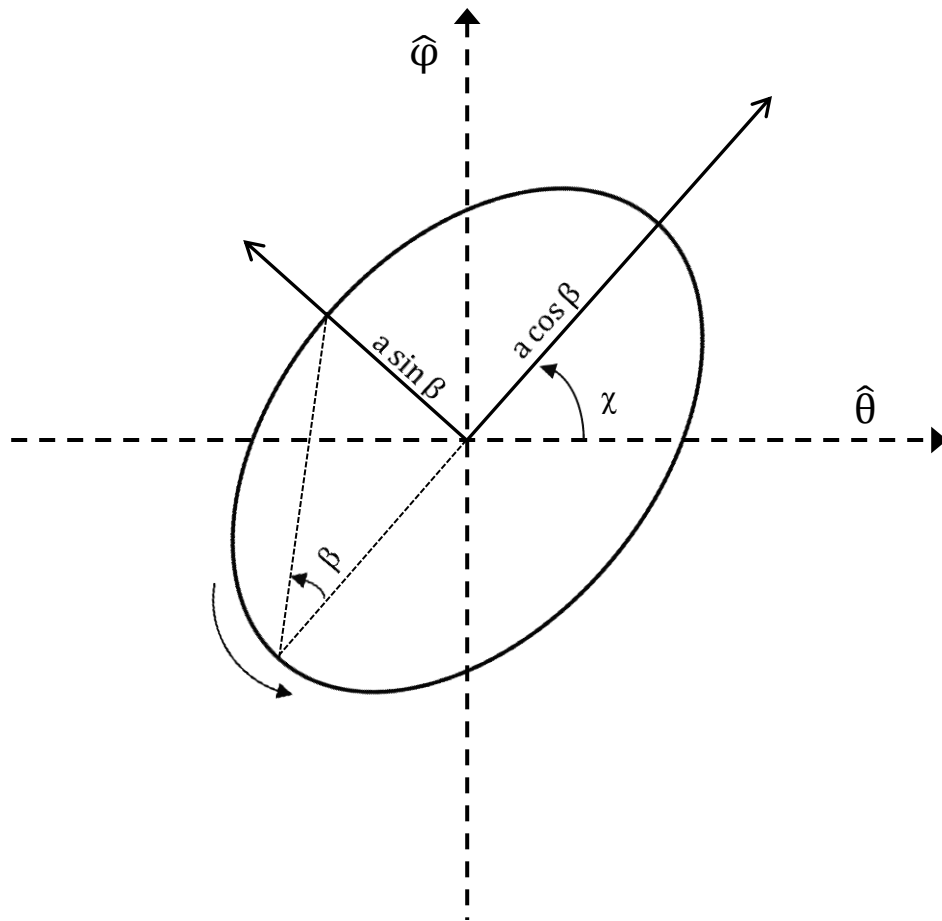
Fig. 6. Polarization ellipse. State of polarization as described by parameters of a simple elliptically polarized beam, rotating in the counter-clockwise direction. This is right-handed polarization and direction of propagation in this case is into the paper ($\hat{\varphi} \times \hat{\theta}$).

It is important to note here that the convention for right and left-circular polarization varies widely in the literature; see van de Hulst [22], Chandrasekhar [21], Hovenier [36], and others for one convention where the direction of rotation of the electric field vector is observed looking down the beam as it propagates away from the observer. I will follow the convention of Bohren and Huffman [35], who define the direction of rotation viewed as a beam of radiation propagates toward an observer. This means that right-circular polarized light will appear to rotate in the clockwise direction as it propagates toward the observer. The conventions in Bohren and Huffman will also be followed for linearly polarized radiation. Fig. 7 summarizes the different states of polarization and their associated Stokes vectors.

One thing must be mentioned about the derivation of the Stokes parameters. It is understood that all the quantities are *time averages*, because measurable quantities are always going to be composed of superpositions of many waves on extremely short timescales. In other words, the amplitudes and phases of the electric field components which were assumed to be invariant in time are actually varying rapidly. This means that in general light is partially polarized and we have the following relation:

$$I^2 \geq Q^2 + U^2 + V^2 \,. \tag{22}$$

If the amplitudes and phases are correlated in time, then the light is said to be fully polarized and the previous inequality becomes an equality.

A degree of polarization can be defined as:

$$\text{DOP} = \frac{\sqrt{Q^2 + U^2 + V^2}}{I} \tag{23}$$

and the degree of linear polarization as:

$$\text{DLP} = \frac{\pm\sqrt{Q^2+U^2}}{I} \, .$$

(24)

The degree of linear polarization will be used in the definition of polarized reflectance

for remote sensing, introduced in a later section. For a discussion of the sign of the linear

polarization, see Appendix B.
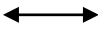
$0°$ $\longleftrightarrow$ $\begin{bmatrix}1\\1\\0\\0\end{bmatrix}$	$90°$ $\updownarrow$ $\begin{bmatrix}1\\-1\\0\\0\end{bmatrix}$	$+45°$ $\nwarrow\searrow$ $\begin{bmatrix}1\\0\\1\\0\end{bmatrix}$
$-45°$ $\nearrow\swarrow$ $\begin{bmatrix}1\\0\\-1\\0\end{bmatrix}$	Right $\begin{bmatrix}1\\0\\0\\1\end{bmatrix}$	Left $\begin{bmatrix}1\\0\\0\\-1\end{bmatrix}$

Fig 7. Stokes parameters of polarized light. Handedness is determined looking toward a
beam of light propagating in the direction of the observer.

The principle of optical equivalence as stated by van de Hulst [22] is that if two

beams have the same Stokes parameters, there is no experimental way to distinguish

them, even if they were formed by interaction with different media. What this means is

that the Stokes parameters are the complete set of quantities needed to define

experimentally the intensity and state of polarization of a beam of radiation. There can

be further theoretical differences, but these do not correspond to anything physically measurable.

The Stokes parameters of multiple incoherent beams may be added together if there is no phase relationship between them, which is very important where multiple scattering is considered because there may be contributions of many beams to the outgoing beam in a certain solid angle. When an incident Stokes vector interacts with the constituents of a medium, the medium changes the Stokes vector and produces a new, or scattered, Stokes vector. The change in the Stokes vector from interaction with the medium can be described by a 16-element 4x4 matrix, called a transformation matrix F by van de Hulst [22], and when normalized, called the scattering phase matrix or Mueller matrix M [37]. The basic equation is of the form:

$$\begin{bmatrix} I_s \\ Q_s \\ U_s \\ V_s \end{bmatrix} = M(\mu, \mu', \varphi - \varphi') \begin{bmatrix} I_0 \\ Q_0 \\ U_0 \\ V_0 \end{bmatrix}, \qquad (25)$$

where the subscript s is for the scattered Stokes vector. The Mueller matrix contains all information about the medium at the specified wavelength and viewing geometry. All 16 elements of the Mueller matrix may be retrieved in an experiment with 49 intensity measurements [38], but often many of the elements are not independent of each other or may be zero if there is symmetry in the system.

In the adding-doubling radiative transfer model used in this study, the Mueller matrix of the ice cloud may be determined by considering four different incident states of radiation: a Stokes vector of [1,0,0,0] (written horizontally here for convenience), corresponding to unpolarized light, a Stokes vector of [1,1,0,0], corresponding to light

polarized at $0°$, a Stokes vector of $[1,0,1,0]$, corresponding to light polarized at $+45°$, and

a Stokes vector of $[1,0,0,1]$, corresponding to right-circularly polarized light. The first

column in the Mueller matrix (elements $M_{11} - M_{41}$) is simply the scattered Stokes vector

corresponding to the incident $[1,0,0,0]$ state, the second column is the scattered Stokes

vector corresponding to the $[1,1,0,0]$ state minus the scattered Stokes vector from the

$[1,0,0,0]$ state, and so on. The full Mueller matrix may be built from the scattered Stokes

vectors that correspond to each of the incident Stokes vectors given [39].

The Vector Radiative Transfer Equation

Now almost all the necessary steps have been taken to include a treatment of

polarization in the radiative transfer equation. The phase function from the scalar

radiative transfer equation (c.f. Eq. 10) is now replaced by a 4x4 scattering matrix. This

is just the product of the single scattering Mueller matrix and two rotation matrices,

which serve to first rotate the incident Stokes vector into the scattering plane (a plane

containing the incident and scattered directions) where the Mueller matrix acts on it,

then to rotate the scattered Stokes vector into the meridian plane (defined in an earlier

section) of the scattered beam. In equation form, the scattering of an incident Stokes

vector (denoted here by **I**) is:

$$\mathbf{I_s} = \mathbf{R}(\pi - \alpha_2)\mathbf{M}(\Theta)\mathbf{R}(-\alpha_1)\mathbf{I_0} \ . \tag{26}$$

The terms on the right side are applied from right to left, meaning the angle α_1 is the

rotation angle from the meridian plane into the scattering plane, and the angle α_2 is the

rotation angle from the scattering plane into the meridian plane of the scattered Stokes

vector.

The first three terms on the right hand side are the phase matrix $\mathbf{Z}$:

$$\mathbf{Z}(\theta, \varphi, \theta', \varphi') = \mathbf{R}(\pi - \alpha_2)\mathbf{M}(\Theta)\mathbf{R}(-\alpha_1) \ . \tag{27}$$

$\mathbf{M}(\Theta)$ is just the 16-element single scattering Mueller matrix defined earlier:

$$\mathbf{M}(\Theta) = \begin{bmatrix} M_{11} & M_{12} & M_{13} & M_{14} \\ M_{21} & M_{22} & M_{23} & M_{24} \\ M_{31} & M_{32} & M_{33} & M_{34} \\ M_{41} & M_{42} & M_{43} & M_{44} \end{bmatrix}, \tag{28}$$

and the rotation matrix $\mathbf{R}$ is the following, defined by van de Hulst [22]:

$$\mathbf{R}(\alpha) = \begin{bmatrix} 1 & 0 & 0 & 0 \\ 0 & \cos 2\alpha & \sin 2\alpha & 0 \\ 0 & -\sin 2\alpha & \cos 2\alpha & 0 \\ 0 & 0 & 0 & 1 \end{bmatrix} . \tag{29}$$

In the process of transfer through a medium, a Stokes vector may go through repeated interactions of the sort in Eq. (26). The final Stokes vector can be represented as the matrix multiplication of the repeated n number of interactions in the following way:

$$\mathbf{I_s} = (\mathbf{Z_n}\mathbf{Z_{n-1}} \dots \mathbf{Z_1})\mathbf{I_0} \ . \tag{30}$$

The product of the n number of phase matrices $\mathbf{Z}$ is called the effective Mueller matrix [40]. Each element of the effective Mueller matrix is usually divided by the M_{11} element so that effects involving polarization can be seen apart from the intensity and is known as the reduced effective Mueller matrix.

Rewriting the radiative transfer equation now, we get:

$$\mu\frac{d\mathbf{I}(\tau,\mu,\varphi)}{d\tau} = \mathbf{I}(\tau, \mu, \varphi) - \mathbf{J}(\tau, \mu, \varphi) \ . \tag{31}$$

The source function is given by:

$$J(\tau, \mu, \varphi) = \frac{\widetilde{\omega}_0}{4\pi} \int_0^{2\pi} \int_{-1}^{1} \mathbf{Z}(\mu, \mu', \varphi - \varphi') \mathbf{I}(\tau, \mu', \varphi') d\mu' \varphi' \ . \qquad (32)$$

$\mathbf{Z}$ is the reduced effective Mueller matrix for the multiple scattering events described in the equation, and $\widetilde{\omega}_0$ is the single scattering albedo introduced earlier, which accounts for the presence of absorption. Eq. (32) gives the full description of electromagnetic radiation including polarization effects in a medium.

CHAPTER IV

AVERAGE SINGLE SCATTERING

AND BULK SCATTERING PROPERTIES

In order to solve the vector radiative transfer equation (VRTE) the single

scattering properties of the medium (the scattering phase matrix) must be determined,

because the VRTE describes a succession of single scattering events that add up to a

total interaction. In this study, the single scattering properties of ice crystals that make

up a cirrus cloud will be determined and used as input to an adding-doubling radiative

transfer model to determine the multiple-scattering output. When calculating the single

scattering properties of the ice crystals, a size distribution is applied, which means that

the scattering properties are weighted for the fraction of ice crystals in each size bin of

the distribution. Different habits (shapes) of crystals and their weights for each size

range are also included in the calculation. Finally, the spectral response function (SRF)

of the satellite sensor must be taken into account, meaning that the average single

scattering properties must be determined over the wavelength range for which the

satellite sensor is sensitive. The PARASOL 0.865 μm (central wavelength) channel will

be used in this study.

Calculating Scattering Properties Using IGOM

Because there is currently no exact method that can be used to calculate

scattering from a large, complicated ice crystal, various approximate methods have to be

used. If the wavelength of the incident light is much smaller than the size of the crystal,

one approach that can be used is the geometric optics method. For this study, the incident wavelength is 0.865 μm, and even the smallest ice crystals considered are at least an order of magnitude larger than the wavelength of the radiation, so the geometric optics method can be used.

Geometric optics considers only plane waves, with the wave front broken up into many small rays that propagate perpendicular to the wave front (so in the same direction as the overall wave). The width between each ray must be smaller than the size of the particle considered, but larger than the wavelength of the incident light, otherwise diffraction due to phase interference breaks down the assumption of a ray as a plane wave [41]. To describe the interaction of a ray with a particle, there are four laws that geometric optics uses: straight-line propagation, reflection, refraction, and the principle of reversibility. This last law says that if a ray is reversed, it will travel in the same path that it took to reach its current point, but in the opposite direction. At each surface of the crystal, a ray can be either reflected or refracted, and the new direction and polarization state depend on the properties of the particle considered and the incident direction. Interactions between the rays can also change the phase of a ray even when the rays are spaced relatively far apart, according to Yang and Liou [42], so this effect is taken into account.

The diffraction of light causes a large increase of scattered energy in the forward direction from an ice crystal which must be taken into account but is not considered in geometric optics. Diffraction occurs when light rays are "bent" around a particle and focused into the forward direction, an effect especially important for larger particles.
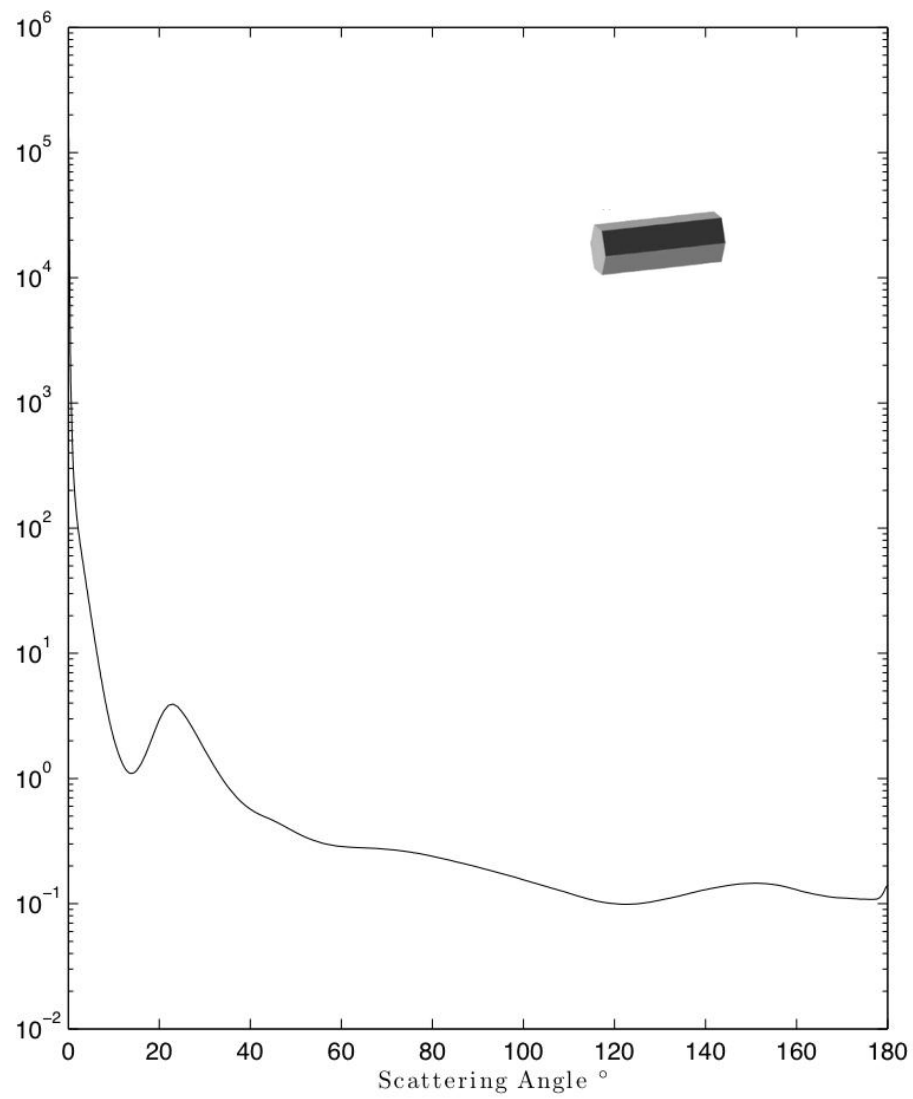
Fig. 8. Phase function of a solid hexagonal column crystal. A size distribution of D_{eff} = 90 μm was used.

A typical phase function, or scattered energy at each scattering angle, is shown in Fig. 8. Notice how much larger the forward peak of the phase function is than the other directions. For many non-spherical ice crystals, the forward peak can be 5-10 orders of magnitude larger than the energy in the other directions. The improved geometric optics method described below does include a treatment of diffraction, unlike conventional geometric optics.

Yang and Liou [43] used a ray-by-ray integration algorithm to solve for the scattered electric field in the far-field zone by integrating the near-field electric field solution inside the particle from the geometric optics method. This method solves for the full scattered field and the extinction and absorption cross sections, from which the single scattering albedo can be obtained. The combined algorithm is called the Improved Geometric Optics Method. Yang and Liou demonstrated that the results compare well with a reference finite-difference time domain (FDTD) result for size parameters down to 20 [43].

As detailed in Bi et al. [14], improvements have been made to the IGOM model, especially for the treatment of rays that pass through two opposing facets of a crystal in the forward direction. The mapping of the near-field to the far-field described in the ray-by-ray integration method was improved with a new way to treat polarized ray spreading and made the δ-transmission term for forward scattering through these faces unnecessary. The phase function at backscattering angles was also improved, along with the efficiency factors [14].

Surface roughness was also added to the model. In Yang et al. [18] two approaches were compared, one a rigorous ray-tracing scheme where each external ray reflected from a roughness facet or emerging internal ray from a roughness facet was tracked to see if it impinged on another roughness facet. All these interactions take significant computational time, so another approach was used where the normal to the surface for each reflection or refraction event was changed randomly. Multiple external reflections and refractions from roughness facets are not taken into consideration in the second approach. Even with this approximation, the two methods compared well, so the second method was employed in calculations [18]. Three different levels of surface roughness were used: none, moderately rough, and severely rough. The spatial orientations of the rough surfaces can be described by a Gaussian distribution with a parameter σ that describes the level of roughness. Smooth particles have $\sigma = 0$, moderately roughened particles have $\sigma = 0.03$, and severely roughened particles have $\sigma = 0.5$. The roughness features are small compared to the size of the particle, but still large enough to have an effect on the incident beam [18]. The effect of surface roughness is to smooth out the phase function and make it almost featureless, removing all of the halo peaks for $\sigma = 0.5$ and all halo peaks except 22° for $\sigma = 0.03$. Sharp halo peaks are not seen in remote sensing measurements and surface roughness could be the reason why [10].

Calculation of Single Scattering Properties

Now a detailed description of the calculation of the single scattering phase matrix can be given. Consider an arbitrary ice crystal for which the scattering properties are

sought using IGOM. An incident ray will have some amplitude and phase with respect to an initial reference plane, while a scattered ray will have another amplitude and phase with respect to the scattering plane.

The necessary tools to describe this transition are given by van de Hulst [22], in the form of four complex functions:

$$S = \begin{bmatrix} S_2 & S_3 \\ S_4 & S_1 \end{bmatrix}.$$ (32)

These functions describe the transition of the electric field from one state to another. As noted in Liou [13], most of the time the far-field solution is the one desired, where kr >> 1. The scattered electric field then becomes (c.f. Eq. (16)) [22]:

$$\begin{bmatrix} E_{\parallel}^s \\ E_{\perp}^s \end{bmatrix} = \begin{bmatrix} S_2 & S_3 \\ S_4 & S_1 \end{bmatrix} \frac{\exp(-ikr+ikz)}{ikr} \begin{bmatrix} E_{\parallel}^0 \\ E_{\perp}^0 \end{bmatrix}.$$ (33)

The functions S depend on the incident and outgoing directions θ and the orientation of the ice crystal with respect to the incoming beam. The 16-element transformation matrix for the Stokes parameters mentioned earlier is a function of these amplitude functions S. This transformation matrix [22] when normalized is called the scattering phase matrix [13]. The scattering phase matrix is proportional to the single scattering Mueller matrix, as discussed earlier.

The scattered Stokes parameters can then be written:

$$\begin{bmatrix} I_s \\ Q_s \\ U_s \\ V_s \end{bmatrix} = \frac{\sigma_s \mathbf{P}}{4\pi r^2} \begin{bmatrix} I_0 \\ Q_0 \\ U_0 \\ V_0 \end{bmatrix},$$ (34)

where **P** is the scattering phase matrix, and σ_s is the scattering cross section which

denotes the fraction of energy scattered out of the beam.

The scattering cross section can be obtained with the following formula, which simply

integrates the intensity over all scattering angles:

$$\sigma_s = \frac{1}{k^2} \int_0^{2\pi} \int_0^{\pi} \left(E_\parallel^s E_\parallel^{s*} + E_\perp^s E_\perp^{s*} \right) \sin\theta \, d\theta d\varphi \ . \tag{35}$$

The scattering phase matrix is of the following form:

$$\mathbf{P}(\Theta, \alpha, \beta) = \begin{bmatrix} P_{11} & P_{12} & P_{13} & P_{14} \\ P_{21} & P_{22} & P_{23} & P_{24} \\ P_{31} & P_{32} & P_{33} & P_{34} \\ P_{41} & P_{42} & P_{43} & P_{44} \end{bmatrix} . \tag{36}$$

P is therefore a function of the incident and outgoing directions and the orientation of the

ice crystal with respect to the incident direction, given by the angles α and β.

To simplify the scattering phase matrix, we follow the discussion given by van de Hulst

[22]. In a sample of randomly oriented ice crystals of the same size, symmetry

relationships exist that will cancel many terms. First, to find a form of the scattering

phase matrix that does not depend on the orientation of the crystal, the integration is

performed over all ice crystal orientations:

$$\mathbf{P}(\Theta) = \frac{1}{2\pi\sigma_s} \int_0^{2\pi} \int_0^{\frac{\pi}{2}} \mathbf{P}(\Theta, \alpha, \beta) \sigma_s(\alpha, \beta) \sin\alpha \, d\alpha \, d\beta \ . \tag{37}$$

The scattering cross section becomes:

$$\sigma_s = \frac{1}{2\pi} \int_0^{2\pi} \int_0^{\pi} \sigma_s(\alpha, \beta) \sin\alpha \, d\alpha \, d\beta \ . \tag{38}$$

The next simplification is symmetry. For a given particle position, there are three other

positions where the scattering phase matrix can be expressed in the same terms as the

initial position. The first is the reciprocal position of the original, which is a rotation about the line that bisects the supplement to the scattering angle (called the "bisectrix" by van de Hulst). The second is the mirror image with respect to the bisectrix plane, and the third is the mirror image with respect to the scattering plane. Assuming that the volume has an equal number of all orientations, the scattering phase matrix reduces to the following form:

$$\mathbf{P}(\Theta) = \begin{bmatrix} P_{11} & P_{12} & 0 & 0 \\ P_{12} & P_{22} & 0 & 0 \\ 0 & 0 & P_{33} & -P_{43} \\ 0 & 0 & P_{43} & P_{44} \end{bmatrix}. \tag{39}$$

The P_{11} element is normalized as in Eq. (4), and the other elements of the scattering phase matrix are normalized by the P_{11} element. This is the form of the scattering phase matrix which IGOM will produce for each size and shape of ice crystal.

Average and Bulk Scattering Properties

The next step in deriving scattering properties to use in the adding-doubling radiative transfer model is to consider size and habit distributions along with the response function of the sensor used and the solar flux at those wavelengths. The bulk properties describe a volume in a general circulation model [44], and so the scattering properties of all the different crystals that make it up must be averaged together to get something that describes the whole collection. The average scattering properties are what we need as input to the adding-doubling radiative transfer model used in this study, so the single scattering properties of different sizes and shapes of ice crystals will be averaged together to produce the average scattering phase matrix and other parameters needed as input.

The average scattering cross section and extinction cross section as given in

Baum et al. [45] are (c.f. Eq. (34)):

$$\sigma_{s,e} = \frac{\int_{\lambda_1}^{\lambda_2} \int_{D_{min}}^{D_{max}} [\sum_{h=1}^{M} \sigma_{s,e,h}(D,\lambda) f_h(D)] n(D) F_s(\lambda) S(\lambda) dD d\lambda}{\int_{\lambda_1}^{\lambda_2} \int_{D_{min}}^{D_{max}} [\sum_{h=1}^{M} f_h(D)] n(D) F_s(\lambda) S(\lambda) dD d\lambda} , \quad (40)$$

where the subscripts s and e on the cross section σ indicate scattering and extinction,

respectively. The sum over h is for different habits in the mixture of ice crystals, and the

habit fraction $f_h(D)$ is defined so that:

$$\sum_{h=1}^{M} f_h(D) = 1 , \quad (41)$$

where M is the number of habits, D is the particle diameter, n(D) is the density, $F_s(\lambda)$ is

the spectral response function (SRF), and $S(\lambda)$ is the solar flux.

The SRF describes how sensitive the satellite sensor is at each wavelength in its

domain. Fig. 9 shows the PARASOL spectral response function for the 0.865 μm band.

The 0.865 μm band on the PARASOL satellite ranges from 0.804 to 0.924 μm, but the

band edges are much less sensitive than the center wavelength. The scattering properties

must be weighted for the wavelengths in the SRF and also for the intensity of the

sunlight seen by the sensor at each wavelength, $S(\lambda)$.

The single scattering albedo $\widetilde{\omega}_0$ is given by the ratio of the scattering to extinction

cross sections:

$$\widetilde{\omega}_0 = \frac{\sigma_s}{\sigma_e} . \quad (42)$$

If there is no absorption, $\sigma_e = \sigma_s$ and $\widetilde{\omega}_0 = 1$.
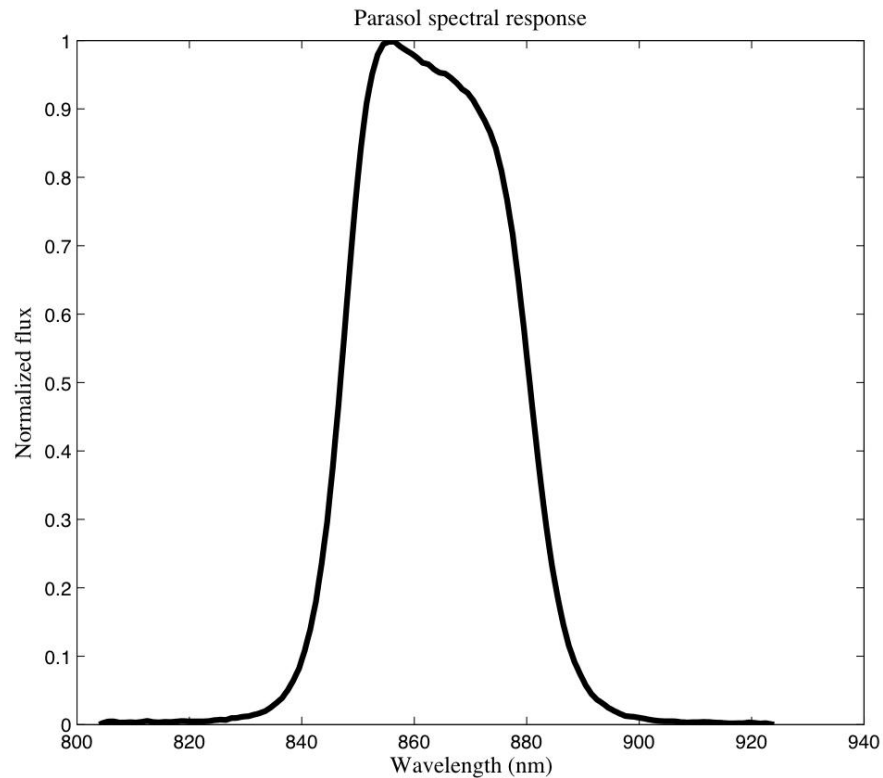
Fig. 9. Spectral Response Function for the 0.865 μm PARASOL band. All values have been normalized to the maximum observed value.

The asymmetry factor g, the first moment of the phase function P_{11}, is just the weighted average of the cosine of the scattering angle for radiation scattered from a certain particle or collection of particles. It is 1 for complete forward scattering (scattering angle of $0^{°}$, $\cos(0) = 1$) and 0 for complete backscattering.

The average asymmetry factor over the particle size distribution and habit distribution is found in the same manner as the scattering cross section above:

$$g = \frac{\int_{\lambda_1}^{\lambda_2} \int_{D_{min}}^{D_{max}} \left[\sum_{h=1}^{M} g_h(D,\lambda)\sigma_{s,h}(D,\lambda)f_h(D)\right]n(D)F_s(\lambda)S(\lambda)dDd\lambda}{\int_{\lambda_1}^{\lambda_2} \int_{D_{min}}^{D_{max}} \left[\sum_{h=1}^{M} \sigma_{s,h}(D,\lambda)f_h(D)\right]n(D)F_s(\lambda)S(\lambda)dDd\lambda}. \quad (43)$$

The average size of the ice crystals in a certain size distribution with certain habits is given by the effective size D_{eff}, defined as the ratio of the total volume to the total projected area [46]:

$$D_{eff} = \frac{3}{2} \frac{\sum_{h=1}^{M}\left[\int_{D_{min}}^{D_{max}} V_h(D)n(h,D)dD\right]}{\sum_{h=1}^{M}\left[\int_{D_{min}}^{D_{max}} A_h(D)n(h,D)dD\right]}. \quad (44)$$

This definition for the average size for each PSD will be employed when discussing results in later sections. Finally, the average single scattering phase matrix is given by:

$$P(\Theta) = \frac{\int_{\lambda_1}^{\lambda_2} \int_{D_{min}}^{D_{max}} \left[\sum_{h=1}^{M} P_h(\Theta,D,\lambda)\sigma_{s,h}(D,\lambda)f_h(D)\right]n(D)F_s(\lambda)S(\lambda)dDd\lambda}{\int_{\lambda_1}^{\lambda_2} \int_{D_{min}}^{D_{max}} \left[\sum_{h=1}^{M} \sigma_{s,h}(D,\lambda)f_h(D)\right]n(D)F_s(\lambda)S(\lambda)dDd\lambda}. \quad (45)$$

The phase matrices for each particle size and shape from Eq. (37) are inserted into the integral above for the computation of the average properties.

PSDs and Habit Fractions Used in Current Study

All the necessary inputs to the adding-doubling radiative transfer program have now been defined. For the current study, five PSDs from the more than 12,000 tabulated from field campaigns [19] were selected for use, which correspond to effective diameters of 10.15 μm, 30.28 μm, 50.42 μm, 70.60 μm, and 90.31 μm. These sizes were selected because Baran and Havemann [47] showed that for cirrus retrieval over ocean D_{eff} varies

between about 30 and 70 μm, and most of the PSDs available for use in this study also fall within that size range. Five models that have different combinations of ice crystal habits will be studied, and the single habits of solid columns and hollow columns will also be studied. Each case considered also has different percentages of crystals for different size ranges; for example, plates might only be considered at large sizes in one case but might be allowed to occur at all size ranges in another case. Each case considered will be studied with crystal surface roughness at either medium or severely rough levels, with the exception being the MODIS C5 model which has all smooth crystals save for the aggregate of columns, which is severely roughened. Smooth crystals are not considered for models except C5 because previous studies have shown that smooth crystals provide a poor fit to polarization measurements [48]. All the details of habits and percentages for each model are shown in the tables in Appendix A. The single habits of hollow columns and solid columns actually have 100% droxtals in the distribution for the smallest sizes of less than 0.001 cm, but exclusively solid or hollow columns for all sizes larger than that.

CHAPTER V

THE PARASOL SATELLITE

PARASOL (Polarization and Anisotropy of Reflectances for Atmospheric Sciences coupled with Observations from a Lidar) is a satellite launched in 2004 to provide information on the radiative and microphysical properties of clouds and aerosols. It carries aboard it a wide-field imaging radiometer/polarimeter called POLDER (POLarization and Directionality of the Earth's Reflectances) which can retrieve the I, Q, and U Stokes parameters at up to 16 viewing angles for each pixel [29]. In the Level-2 processed data, other parameters of interest are available, including surface type, percentage cloud cover, optical depth, and thermodynamic phase. This extra information will be used to select pixels for the current study.

The Polarimeter Concept

The wide-field imager is equipped with a CCD matrix detector and a rotating wheel that has spectral filters and polarizers, allowing it to image at 9 different wavelengths and collect polarization information at three of those wavelengths, including the 0.865 μm channel which will be used in the current study. The I, Q, and U Stokes parameters are derived by collecting three measurements with the polarizer axis turned in steps of $60°$ each time. The spacecraft moves during this time so, to collocate the three measurements, a small angle wedge prism is employed for each polarizer [27].
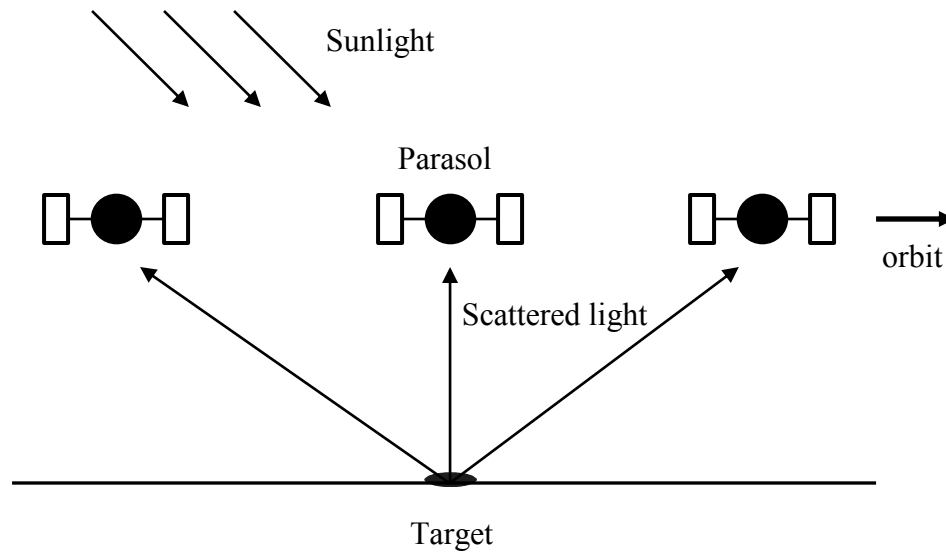
Fig. 10. Viewing geometry of the PARASOL satellite.

Viewing Geometry

As seen in Fig. 10, PARASOL can view the same pixel from many different vantage points as it flies overhead, meaning that it can collect information on the same pixel at a wide range of scattering angles. The viewing zenith angle is defined with respect to the local zenith and varies between $0°$ and $75°$ in observations. The solar zenith angle is also measured from the local zenith and varies between $0°$ and $80°$ in observations, and the relative azimuth angle is measured from the local north direction and varies between $0°$ and $360°$ in observations. With this definition, $180°$ is forward scattering, and $0°$ or $360°$ is backscattering. See Fig. 11 for details.
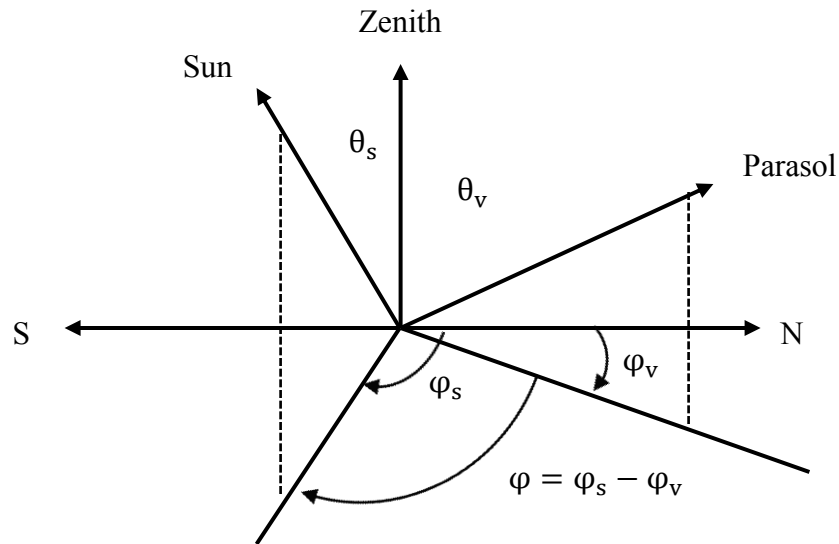
Fig. 11. Coordinate system for PARASOL observations.

The Level-2 Cloud Product

The PARASOL Level-2 cloud product is used in this study. The Level-2 product

contains parameters which are useful in the study of clouds and is obtained by

processing of the Level-1 radiances by CNES (Centre National d'Etudes Spatiales). The

parameters used are percentage cloud cover, surface type, thermodynamic phase, and

normalized, modified, polarized radiance at 0.865 μm. The normalized, modified,

polarized radiance is defined as follows [49]:

$$L_{nmp}(\theta_v, \varphi_v, \theta_s, \varphi_s) = \frac{\pi L_p}{E_s} \frac{\cos \theta_s + \cos \theta_v}{\cos \theta_s}, \tag{46}$$

where subscript s is for the solar zenith and azimuth angles, and subscript v is for the viewing angles. E_s is the incident solar flux at the top of the atmosphere. L_p is the polarized radiance, defined as:

$$L_p = \pm\sqrt{Q^2 + U^2} \ . \qquad\qquad (47)$$

The Stokes parameters obtained from the adding-doubling radiative transfer model will be used to calculate the normalized, polarized radiance in the same manner as above for comparison to the PARASOL measurements.

Additional restrictions are placed on the data used in the current study, including that the range of scattering angles for each pixel must be at least 50°, the number of viewing directions with data (out of the 16 possible directions) must be at least seven, and the pixels must be over the ocean [49]. A pixel is only accepted if it is 100% cloudy and if its phase is marked as ice. Measurements near the solar principal plane (the plane containing the incident solar zenith direction) that fall within the solid angle possibly contaminated with glint from the ocean surface are removed because the polarization is large and could contaminate the results from polarization due to ice clouds. Data from August 1, 2007 are used that come from 15 orbits of the satellite. After applying the necessary filters, about 70,000 data points are left for use in comparison studies with modeled data.

CHAPTER VI

THE ADDING-DOUBLING RADIATIVE TRANSFER MODEL

In the plane-parallel assumption, the adding method and the doubling method are

convenient methods employed to find the vector intensity of scattered radiation from the

top of the layer. Van de Hulst [30] has a good discussion of the adding-doubling method

and presents the basic equations. The adding-doubling model used in this study was

developed at the Free University of Amsterdam astronomy group by de Haan et al. [11]

and gives the vector intensity and polarization of radiation at the top (or bottom) of a

plane-parallel system.

The Adding Method

Often the atmosphere will be simulated as several plane-parallel layers. Consider

a case as in Fig. 12 where there are two layers in the atmosphere. If layer 1 has an optical

depth τ_1 and layer 2 has optical depth τ_2, then by finding the reflection and transmission

matrices (**R**,**T**) of the separate layers, the reflection and transmission matrices of a

combined layer with optical depth $\tau_1 + \tau_2$ can be determined with the adding equations

discussed in a following section.

Normally the reflection and transmission matrices for the separate layers are not

previously known, and the properties of the layers might vary with optical depth (i.e., the

layers are vertically inhomogeneous). In this case, each layer is divided into many

optically thin layers so that each thin layer can be considered homogeneous and can be

approximated with one or two orders of scattering.
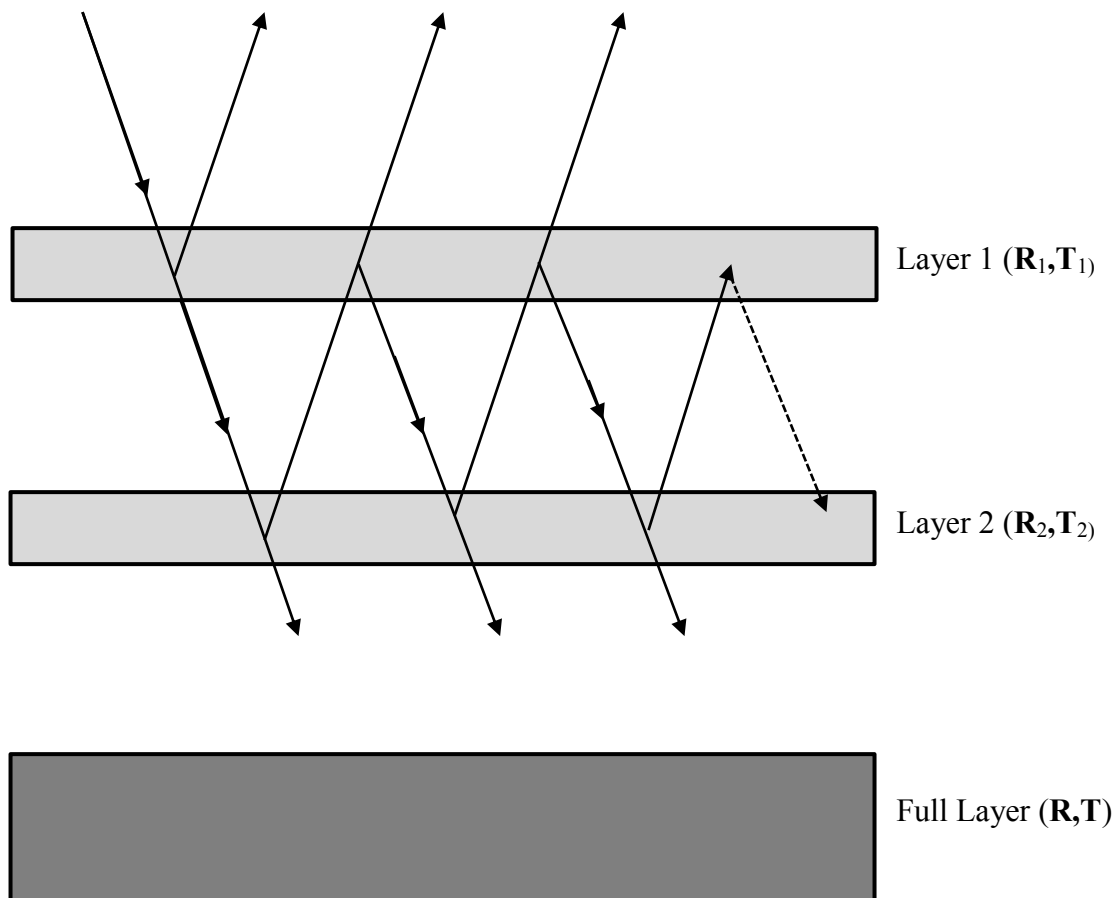
Fig. 12. The adding method. Light coming in from above layer 1 will reflect at layer 1 or transmit through and then reflect at layer 2 or transmit through. There can be reflections between the two layers of an infinite number but they are very weak after a few reflections. The reflection and transmission matrices of the full layer are found from the matrices for the 2 separate layers.

The reflection and transmission matrices are calculated for the thin layers, and the adding equations are used to find the matrices for the combined layer until the combined layers equal the original optical depth of the layer considered. The reflection and transmission matrices of a combination of layers include the infinite reflections that can occur at the interface between the layers, meaning that multiple scattering is included in the model.

The Doubling Method

When the properties of the layer considered do not vary with optical depth, then the doubling method is a faster way to calculate reflection and transmission. Since the thin layers sliced from the large layer have the same properties, the initial reflection and transmission matrices do not have to be re-calculated each time. The layers may simply be added two at a time until the optical depth of the original layer, before division into thin layers, is reached. This is clearly a special case of the adding method and does not employ any different equations in its calculations. The original layer must be divided into thin layers of equal optical depth for this method to work, otherwise, the reflection and transmission matrices would not be the same for each thin layer.

In the present study, we used a four-level atmosphere with a different optical depth for each layer and a Lambertian ocean surface with albedo 0.06. The vertical distribution of gases is given by the Air Force Geophysics Laboratory atmospheric profile [50], and the Rayleigh scattering depolarization factor used in the adding-doubling model is 0.0279, as reported in Young [51]. The Rayleigh optical depth for each layer is calculated from the tables in Tomasi et al. [52]. Each individual layer is

vertically homogeneous, however, so the doubling method may be employed to calculate the reflection and transmission matrices, and the adding equations can be used to obtain the matrices for the full optical depth.

The Equations for Adding and Doubling

This discussion follows de Haan et al. [11], and a more detail can be found there. To track radiation propagating upward and downward in the atmosphere, de Haan introduced the matrices $\mathbf{U}(\tau, \mu, \mu', \varphi - \varphi')$ and $\mathbf{D}(\tau, \mu, \mu', \varphi - \varphi')$ which are defined through the following equations:

$$\mathbf{I}(\tau, -\mu, \varphi) = \frac{1}{\pi} \int_0^{2\pi} \int_0^1 \mathbf{U}(\tau, \mu, \mu', \varphi - \varphi') \mathbf{I}(0, \mu', \varphi') \mu' d\mu' d\varphi' \quad , \tag{48}$$

$$\mathbf{I}(\tau, \mu, \varphi) = \frac{1}{\pi} \int_0^{2\pi} \int_0^1 \mathbf{D}(\tau, \mu, \mu', \varphi - \varphi') \mathbf{I}(0, \mu', \varphi') \mu' d\mu' d\varphi'$$

$$+ \exp\left[-\frac{\tau}{\mu}\right] \mathbf{I}(0, \mu, \varphi) \quad , \tag{49}$$

where $\mathbf{I}(0, \mu, \varphi)$ is the incident intensity at the top of the atmosphere. These equations give the upward and downward intensity, respectively, as a function of optical depth. The exponential term in Eq. (49) represents the unscattered light that reaches an optical depth τ. For light incident on the lower boundary of the atmosphere, analogous equations can be defined but are not shown here.

The problem to be solved is to determine the $\mathbf{U}$ and $\mathbf{D}$ matrices from the albedo $\tilde{\omega}_0$ and phase matrix $\mathbf{Z}(\tau, \mu, \mu', \varphi - \varphi')$. $\mathbf{Z}$ is the phase matrix as defined in the meridian plane through a rotation, as shown in Chapter III. These matrices will be determined with the adding equations using $\tilde{\omega}_0$ and $\mathbf{Z}$.

The light at the top or bottom of the atmosphere is generally desired, and so $\mathbf{U}$ and $\mathbf{D}$ are determined by their boundary values. The boundary values are known as the reflection and transmission matrices and are given by the following equations:

$$\mathbf{T}(\mu, \mu', \varphi - \varphi') = \mathbf{D}(\tau', \mu, \mu', \varphi - \varphi')$$

$$\mathbf{R}(\mu, \mu', \varphi - \varphi') = \mathbf{U}(0, \mu, \mu', \varphi - \varphi')$$

$$\mathbf{T}^*(\mu, \mu', \varphi - \varphi') = \mathbf{D}^*(0, \mu, \mu', \varphi - \varphi')$$

$$\mathbf{R}^*(\mu, \mu', \varphi - \varphi') = \mathbf{U}^*(\tau', \mu, \mu', \varphi - \varphi') . \tag{50}$$

The asterisk indicates radiation incident from below the layer, and τ' is the entire optical depth, with $\tau = 0$ being the top of the layer. With the assumption of no reflecting surface and homogeneous layers where multiple scattering can be neglected (thin layers), the reflection and transmission matrices are found in the following way:

$$\mathbf{R}(\mu, \mu', \varphi - \varphi') = \frac{\tilde{\omega}_0}{4(\mu+\mu')} \mathbf{Z}(\mu, \mu', \varphi - \varphi')\left(1 - \exp\left[-\tau'\left(\frac{1}{\mu} + \frac{1}{\mu'}\right)\right]\right), \tag{51}$$

$$\mathbf{T}(\mu, \mu', \varphi - \varphi') = \frac{\tilde{\omega}_0}{4(\mu+\mu')} \mathbf{Z}(\mu, \mu', \varphi - \varphi')\left(\exp\left[-\tau'\left(\frac{1}{\mu}\right)\right] - \exp\left[-\tau'\left(\frac{1}{\mu'}\right)\right]\right), \text{ if } \mu \neq \mu'$$

$$\mathbf{T}(\mu, \mu', \varphi - \varphi') = \frac{\tilde{\omega}_0 \tau'}{4\mu^2} \mathbf{Z}(\mu, \mu', \varphi - \varphi')\exp\left[-\tau'\left(\frac{1}{\mu}\right)\right] . \tag{52}$$

The repeated reflections are determined from the following three equations:

$$\mathbf{Q}_1(\mu, \mu', \varphi - \varphi') = \frac{1}{\pi}\int_0^{2\pi}\int_0^1 \mathbf{R}'^*(\mu, \mu'', \varphi - \varphi'')\mathbf{R}''(\mu'', \mu', \varphi'' - \varphi')\mu''d\mu''d\varphi''$$

$$\mathbf{Q}_{n+1}(\mu, \mu', \varphi - \varphi') = \frac{1}{\pi}\int_0^{2\pi}\int_0^1 \mathbf{Q}_1(\mu, \mu'', \varphi - \varphi'')\mathbf{Q}_n(\mu'', \mu', \varphi'' - \varphi')\mu''d\mu''d\varphi''$$

$$\mathbf{Q}(\mu, \mu', \varphi - \varphi') = \sum_{n=1}^{\infty} \mathbf{Q}_n(\mu, \mu', \varphi - \varphi') , \tag{53}$$

where a single prime indicates the top layer, and a double prime indicates the bottom layer. The first equation for $\mathbf{Q}_1$ just integrates over all solid angles the reflection matrix

from the bottom layer due to radiation coming from above multiplied by the reflection matrix from the top layer due to radiation from below. This integration calculates the contribution of scattering in the direction (μ, φ). The sum over $\mathbf{Q}_n$ adds all the reflections between the two layers and keeps track of the number of times n that the beam crosses the combined layer in the upward direction.

The matrices $\mathbf{D}$ and $\mathbf{U}$ for radiation propagating downward and upward in the combined layer can then be expressed as:

$$\mathbf{D} = \mathbf{T} + \mathbf{Q} \exp\left[-\tau'\left(\frac{1}{\mu'}\right)\right] + \mathbf{QT}$$

$$\mathbf{U} = \mathbf{R} \exp\left[-\tau'\left(\frac{1}{\mu'}\right)\right] + \mathbf{RD} . \tag{54}$$

Identical (same thickness and scattering properties) and homogeneous layers have been considered here, and the notation has been simplified so that the last terms in both equations are actually an integration just like in Eq. (53).

The reflection and transmission matrices for the combined layer can then be calculated using the following formulas:

$$\mathbf{R}(\mu, \mu', \varphi - \varphi') = \mathbf{R}(\mu, \mu', \varphi - \varphi') + \mathbf{U}(\tau', \mu, \mu', \varphi - \varphi') \exp\left[-\tau'\left(\frac{1}{\mu}\right)\right]$$

$$+ \frac{1}{\pi} \int_0^{2\pi} \int_0^1 \mathbf{T}^* (\mu, \mu'', \varphi - \varphi'') \mathbf{U}(\tau', \mu'', \mu', \varphi'' - \varphi') \mu'' d\mu'' d\varphi'' , \tag{55}$$

$$\mathbf{T}(\mu, \mu', \varphi - \varphi') = \mathbf{T}''(\mu, \mu', \varphi - \varphi') \exp\left[-\tau'\left(\frac{1}{\mu'}\right)\right] + \mathbf{D}(\tau', \mu, \mu', \varphi - \varphi') \exp[-\tau'\left(\frac{1}{\mu}\right)]$$

$$+ \frac{1}{\pi} \int_0^{2\pi} \int_0^1 \mathbf{T}''(\mu, \mu'', \varphi - \varphi'') \mathbf{D}(\tau', \mu'', \mu', \varphi'' - \varphi') \mu'' d\mu'' d\varphi'' . \tag{56}$$

As noted in de Haan [11], a separate adding scheme to obtain **R*** and **T*** is not

necessary since they can be obtained by the symmetry relations

$$\mathbf{R}^*(\mu, \mu', \varphi - \varphi') = \mathbf{R}(\mu, \mu', \varphi' - \varphi)$$

$$\mathbf{T}^*(\mu, \mu', \varphi - \varphi') = \mathbf{T}(\mu, \mu', \varphi' - \varphi) \,. \tag{57}$$

The adding equations, used above for identical homogeneous layers (so actually the

doubling method), are repeatedly applied to add together layers until the optical depth of

the full atmosphere system is reached.

Phase Function Truncation

Since ice crystals are large, diffraction contributes to a peak in scattered energy

in the P_{11} element of the phase matrix, also called the phase function, at the scattering

angle $\Theta = 0°$ (the forward direction). The peak can be many orders of magnitude greater

than in other directions (c.f. Fig. (8)) and is hard to parameterize in the adding-doubling

model.

The adding-doubling code uses Legendre polynomials to represent the phase

function in calculations, because the expansion coefficients are easily determined using

orthogonality relations and can be added together [13]. Because of the forward peak,

many thousands of coefficients are needed in the Legendre polynomial expansion in

order to accurately represent the phase function. This significantly increases the

computational burden [53]. What is needed is a way to represent the phase function with

only a few hundred or even a few dozen terms.

One way to do this is to truncate the forward peak, or remove the scattered

energy in the forward direction. This has the effect of reducing the number of Legendre

coefficients necessary to represent the phase function. The δ-fit truncation method [54], similar to the Delta-M method [53], uses weighted singular-value decomposition least-squares fitting, which better approximates the phase function at large scattering angles. The method finds the coefficients which minimize the squared differences between the true and approximate phase functions.

When the phase function is truncated, the other elements of the phase matrix must be changed in some way to reflect the changes to the P_{11} element. All of the other matrix elements are scaled similar to the following [55]:

$$P_{22}^*(\Theta) = \frac{P_{22}}{P_{11}} P_{11}^*(\Theta) , \tag{58}$$

where the asterisk indicates the truncated element. The optical depth, single scattering albedo, asymmetry factor, and other scattering properties must also be scaled in accordance with the similarity principle [13]. The new asymmetry factor becomes:

$$g^* = \frac{g-f}{1-f} , \tag{59}$$

where f is the fraction of energy in the truncated peak. The single scattering albedo and optical depth are scaled in the following manner:

$$\widetilde{\omega}_0^* = \frac{(1-f)\widetilde{\omega}_0}{(1-f\widetilde{\omega}_0)} , \tag{60}$$

$$\tau^* = (1 - f\widetilde{\omega}_0)\tau . \tag{61}$$

The truncated values of the phase matrix, optical depth, single scattering albedo, asymmetry factor, and other single scattering properties will now be referred to and used in the later parts of this study.

Expansion in Fourier Series

The number of integrations required in the adding method can be reduced by expanding each function dependent on the azimuth angle in a Fourier series, which will greatly shorten the computational time required. The usual expansion is of the following form:

$$\mathbf{Z}(\mu, \mu', \varphi - \varphi') = \sum_{m=0}^{\infty}(2 - \delta_{m,0})[\mathbf{Z}^{cm}(\mu, \mu') \cos m(\varphi - \varphi')$$

$$+ \mathbf{Z}^{sm}(\mu, \mu') \sin m(\varphi - \varphi')] \,, \qquad (62)$$

where $\mathbf{Z}$ can actually be any of the matrices discussed in the context of the adding equations and $\delta_{m,0}$ is the kronecker delta. In order to use this method, the Fourier coefficients must be found. $\mathbf{Z}^{sm}$ and $\mathbf{Z}^{cm}$ can be related to $\mathbf{Z}^m$ through the following equation:

$$\mathbf{Z}^m(\pm\mu, \mu') = (-1)^m \sum_{l=m}^{\infty} \mathbf{P}_m^l (\pm\mu)\mathbf{S}^l\mathbf{P}_m^l(\mu) \,, \qquad (63)$$

where $\mathbf{S}^l$ are the expansion coefficients of the phase matrix in generalized spherical functions, and $\mathbf{P}_m^l$ is a matrix of generalized spherical functions. These functions are the more general version of the Legendre polynomials previously discussed, and follow the same orthogonality and addition relationships. Jackson [20] has a good discussion of these functions.

CHAPTER VII

RESULTS

The adding-doubling model gives the output Stokes vector at the top of the

atmosphere for each viewing geometry, allowing for a full view of radiation scattered

upward from an ice cloud. In the results that follow, the Mueller matrix is displayed on

polar plots, an example of which can be seen in Fig. 13. Fig. 13 is actually a plot of the

scattering angle that corresponds to each point in the Mueller matrix, but the geometry is

the same. The viewing zenith angle θ increases along a radius from $0°$ at the very center

of the figure (looking straight down on an ice cloud) to $90°$ at the edge, while the relative

azimuth angle $(\varphi - \varphi')$ increases from $0°$ to $360°$, where $0°/360°$ corresponds to forward

scattering (both the solar radiation vector and the scattered vector point in the same

direction) and $180°$ corresponds to backscattering. In terms of the relative azimuth angle,

viewing zenith angle, and solar zenith angle, the cosine of the scattering angle can be

expressed in the following way [13]:

$$\cos \Theta = \cos \theta \cos \theta' + \sin \theta \sin \theta' \cos(\varphi - \varphi') , \qquad (64)$$

where θ indicates the viewing zenith angle and θ′ the solar zenith angle.

Four cases are examined in this study: first, the effective Mueller matrices for the

MODIS Collection 5 ice cloud product and a deep convective ice model are investigated.

The second case examines the polarized reflectance for the MODIS C5 model, the four

other ice models, and two single habits at both levels of surface roughness in order to

determine if the new models or single habits have a better polarization fit than the
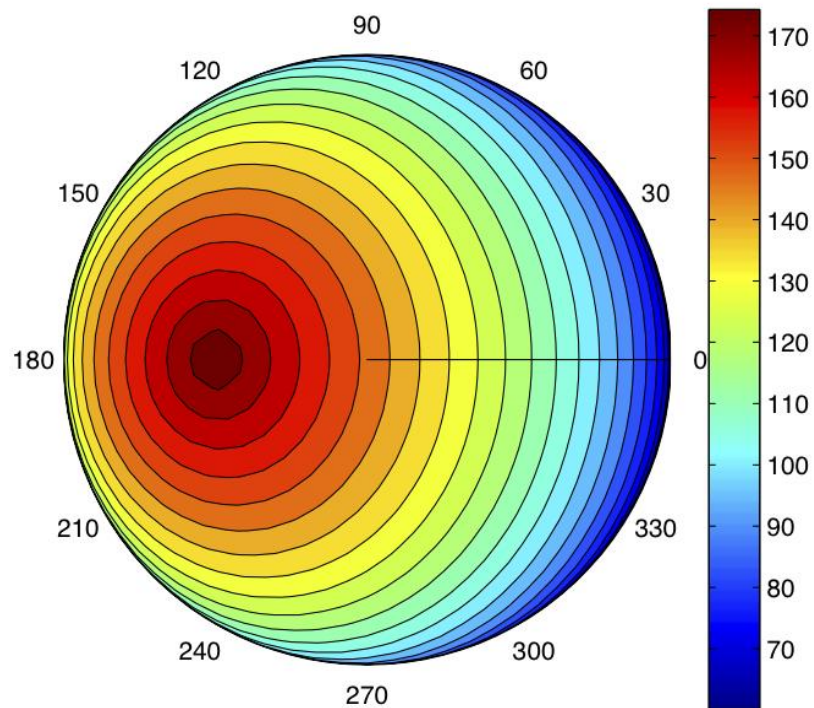
Fig.13. Scattering angle Θ for each viewing geometry of a Mueller matrix. The incident solar zenith angle is $30°$. Note the maximum scattering angle in the principal plane at the viewing angle of $30°$, corresponding to radiation scattered directly back toward the source.

current MODIS model and what level of roughness is appropriate. Dependence of polarized reflectance on effective diameter is examined in the third case, where each ice model is shown at effective diameters from 10-90μm. Finally, the fourth case considers the choice of the best overall ice model, size, and surface roughness level to fit the polarization data from the PARASOL measurements considered. Using information from the first three cases, the best ice model candidates are compared to find the closest fit. The habits and percentages for each ice model may be found in the tables in Appendix A.

Case 1

For this case, the upward radiance from an ice cloud is simulated and the reduced effective Mueller matrix is retrieved to study the sensitivity of the Mueller matrix to the assumed ice microphysical model. Table 2 shows the input parameters to the adding-doubling program that were used. Lawless [33] found that it was hard to distinguish size using an effective Mueller matrix, so for this comparison an effective size of 50 μm is used since it is the median size of the available modeled data. Fig. 14 shows the M_{11} through M_{42} components of the effective Mueller matrix for MODIS C5 and for the deep convective model.

Table 2. Adding-doubling model input for case 1.

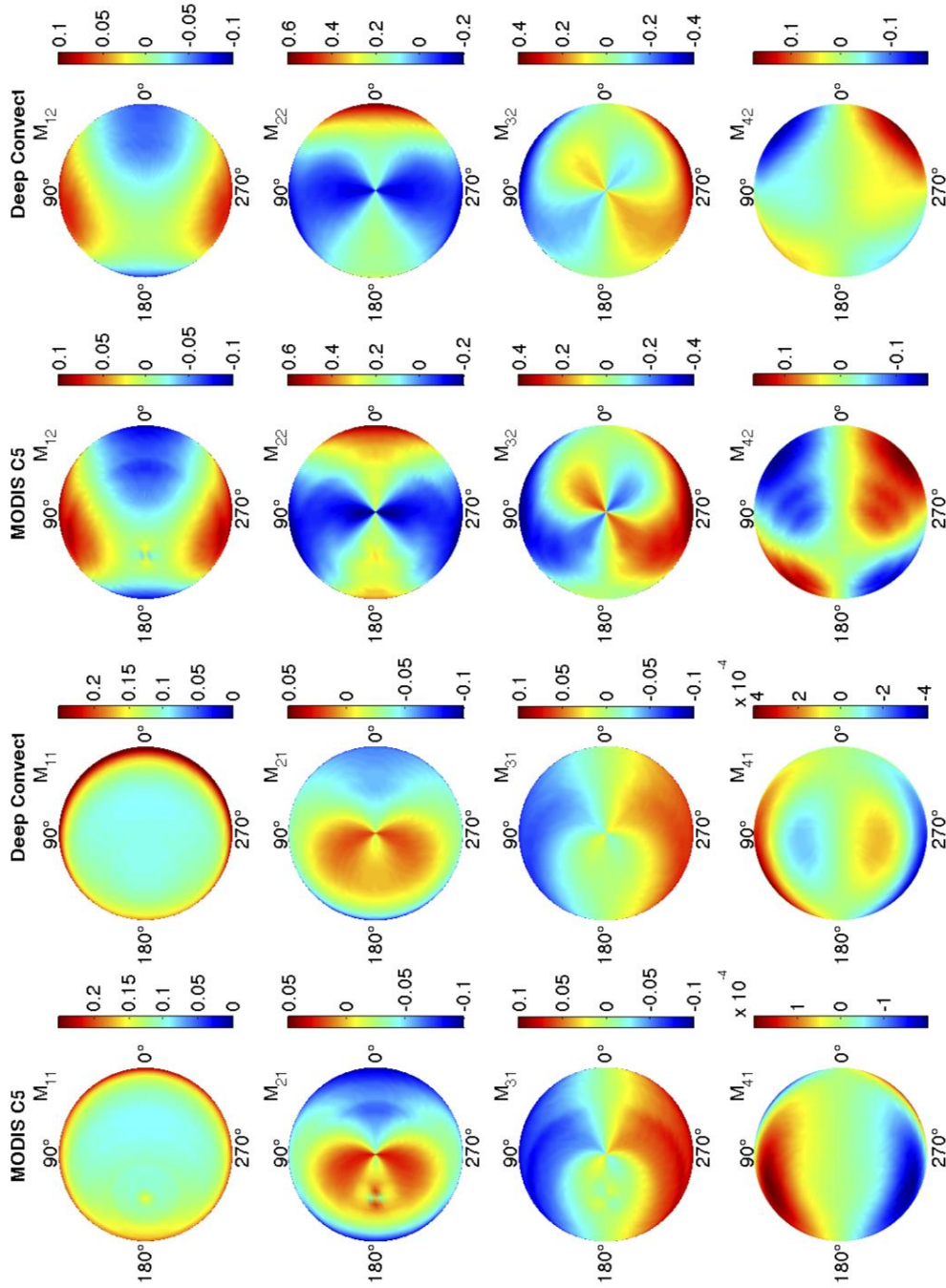|	
Incident Wavelength	$\lambda = 0.865$ μm
Incident Solar Zenith Angle	$\theta = 30°$
Ice Cloud Optical Depth	$\tau = 1.0$

Fig. 14. Elements $M_{11} - M_{42}$ of the effective Mueller matrix. D_{eff} is 50μm.
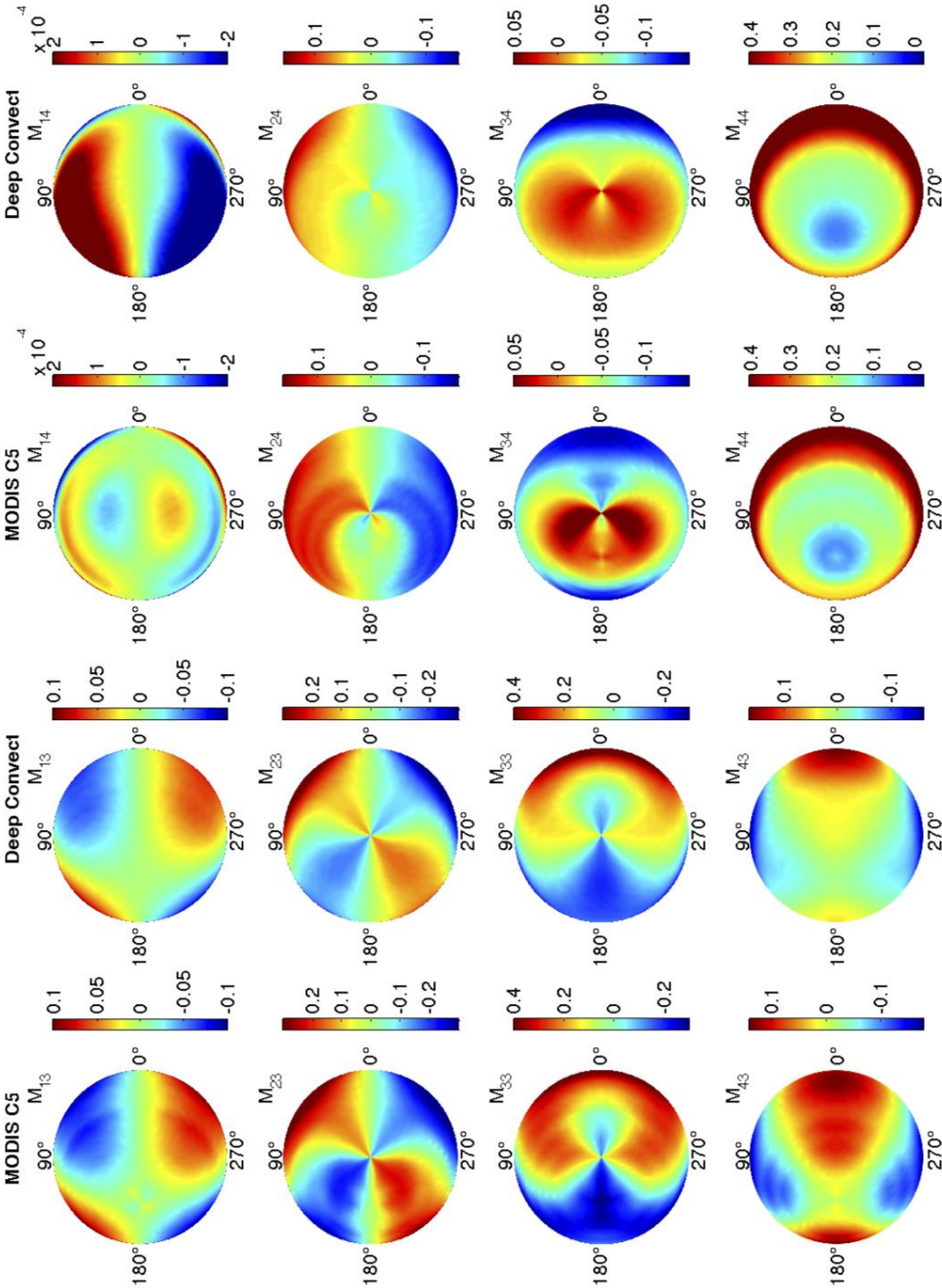
Fig. 15. Elements $M_{13} - M_{44}$ of the effective Mueller matrix. D_{eff} is 50µm.

The elements of the effective Mueller matrix are compared side-by-side for easy reference. Fig. 15 shows the M_{13} through M_{44} components for the same models.

The effective Mueller matrices show some differences between the C5 ice model and the deep convective ice model. There is more forward scattering evident in the M_{11} element, reflecting a lower $180°$ backscattering peak vs. the C5 model in the scattering phase matrix in Fig. 16. All of the scattering phase matrix elements for the deep convective model are smoother than the C5 model due to surface roughness, which tends to wash out features such as the halo peaks at $22°$ and $46°$ in the phase function.

As expected, the M_{44} element is lowest at the scattering angle of $180°$ on the plot. Interestingly, the M_{14} element is noticeably different between the models. Hovenier [56] shows that the scattering phase matrix after rotation from the scattering plane to the meridian plane has zeroes for the top right and lower left elements, but since the Mueller matrix contains the effects of multiple scattering, these elements are non-zero. The difference in the M_{14} element between the two models could show a difference in the amount of multiple scattering occurring. The habit mixture for the deep convective model given in Appendix A shows that a large aggregate of plates makes up 85% of the mix at large sizes, supporting the idea that multiple scattering from the spatially large and complex crystals is reflected in M_{14}.

Multiple scattering will also reduce linear polarization. Taking a look at the M_{12} element of the effective Mueller matrix the deep convective element has slightly lower values than the C5 element, most clearly in the backscattering direction. It is hard to interpret the Mueller matrix from the scattering phase matrix because of rotation of the
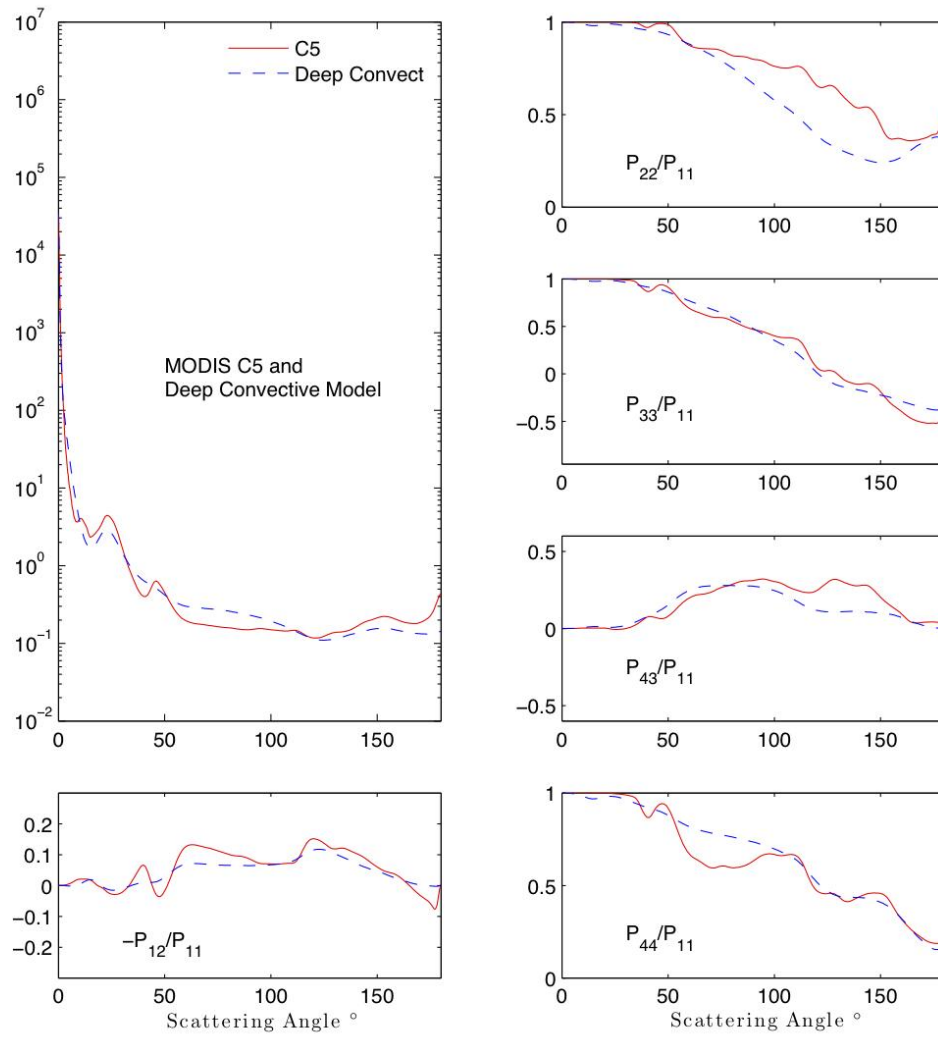
Fig. 16. Scattering phase matrix for MODIS C5 and deep convective models.

reference plane, however. Most of the effective Mueller matrix elements are quite similar between the two models in any case.

The effective Mueller matrices for the other ice models are similar to the C5 model and each other and are not shown here. For ice models containing many different habits, the effective Mueller matrix seems to vary little with changes in the habit percentages, with the exception of the deep convective model which has a high concentration of large branched crystals the other models do not have. The small differences in the Mueller elements between the ice models tested means that it would be difficult to use this tool to distinguish between different habit distributions. The next few cases will test the ice models using polarized reflectance.

Case 2

In this case, the top of atmosphere Stokes vector is simulated from the adding-doubling code using ~1000 geometries at angles which occur in PARASOL satellite observations and the polarized reflectance is derived as described in an earlier section. The optical depth is again 1, and the incident wavelength is 0.865 μm. Comparison is made between polarized reflectance using the MODIS collection 5 ice model, several other ice models, and two single habits, all at D_{eff} = 50 μm for simplicity. Size dependence will be investigated in another case.

Fig. 17 shows the polarized reflectance for C5 and for general model 1 at two levels of surface roughness, moderate and severely rough. C5 has a clear peak near 150° which Model 1 does not have, likely due to the surface roughness of Model 1.
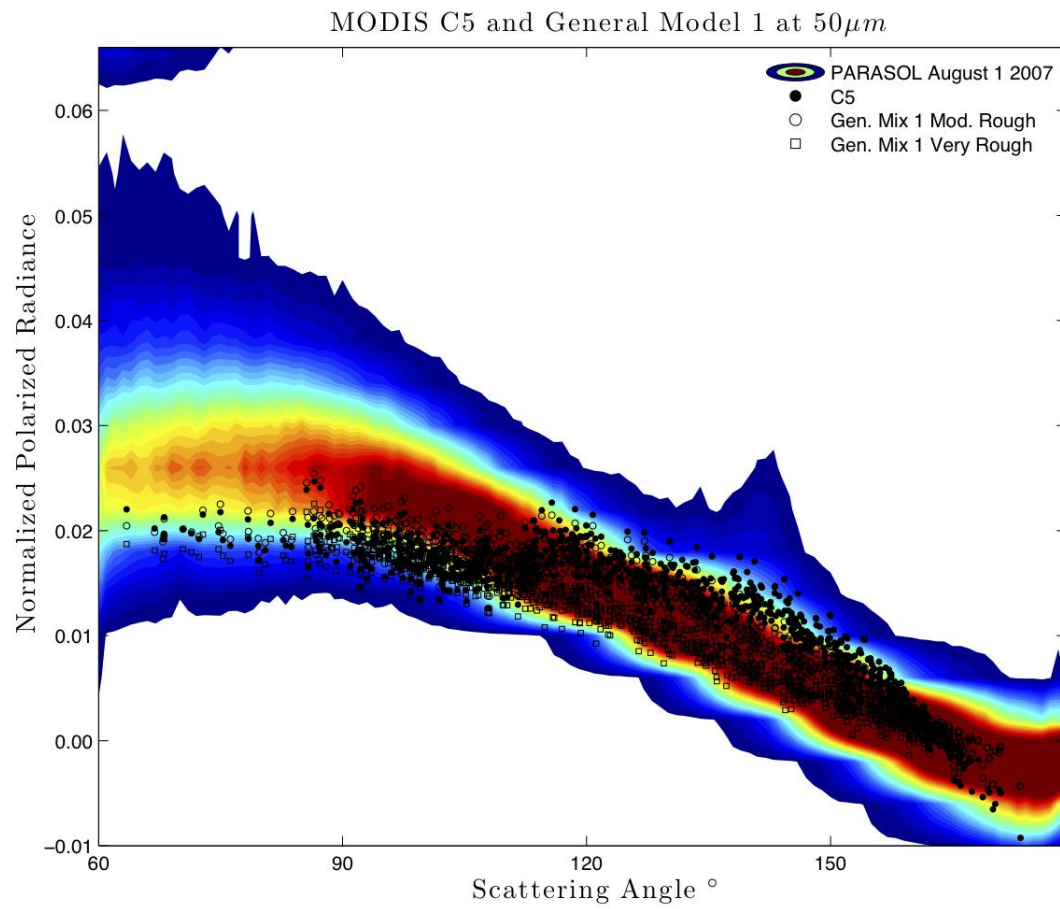
Fig. 17. Polarized reflectance for C5 and general model 1.

A rainbow signal, which is a peak at the scattering angle of $138°$ from spherical water droplets, exists in the PARASOL data and is explained by Baran et al. [48] as a thin layer of cirrus overlaying water clouds, which will show up as ice clouds in the PARASOL phase discrimination algorithm, but because of the optically thin cirrus the rainbow peak will still be detected. The C5 model polarized reflectance is generally too high at large scattering angles and too low at smaller scattering angles, and does not reproduce the negative trend with increasing scattering angle well. General model 1 follows the peak PARASOL polarized reflectance density well at large scattering angles, but is too low at scattering angles from about $60°$ to $100°$. Moderate surface roughness fits the polarization better overall, and for all but the largest scattering angles severe roughness is consistently lower. Going back to Case 1 where the Mueller matrix showed evidence of increased multiple scattering in the deep convective model and decreased linear polarization, the severely roughened surface here seems to be lessening the polarization through more multiple scattering.

The roughened surface is similar to the distortion parameter that Baran et al. [48] used in their study, where they showed that past a certain value, the distortion parameter does not produce a good polarization fit. Some surface roughness is desirable, however, to smooth out sharp features in the P_{11} and $-P_{12}/P_{11}$ elements of the phase matrix which do not strongly show up in remote sensing measurements, such as the $22°$ and $46°$ halos, along with the $180°$ backscatter peak.
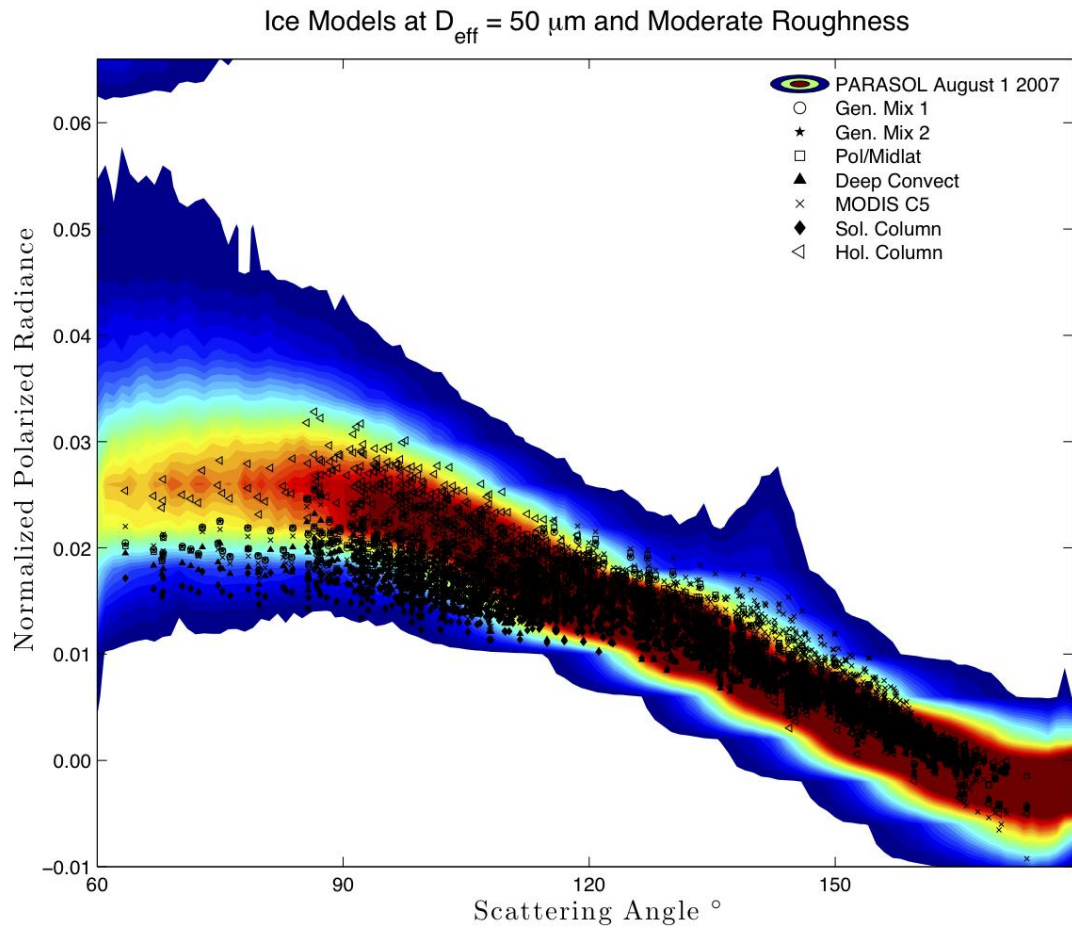
Fig. 18. All models plotted together at moderate surface roughness.
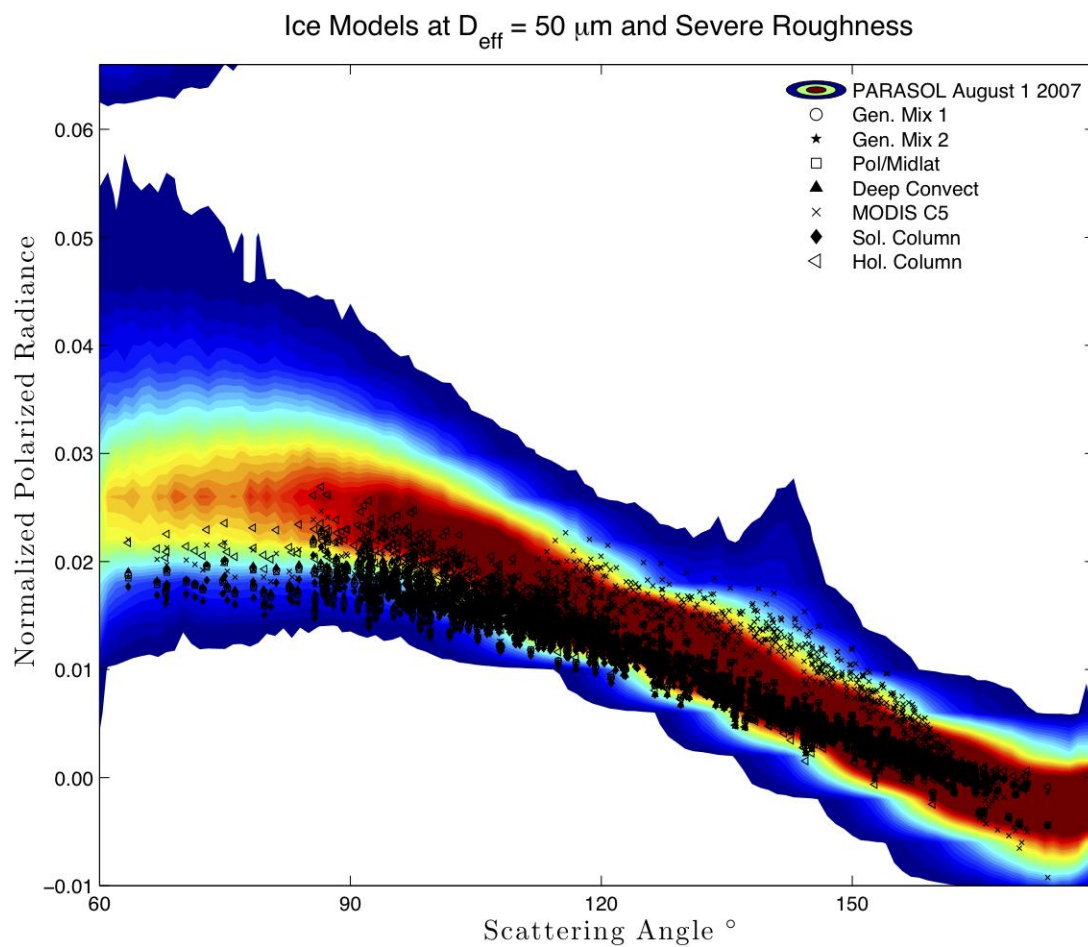
Fig. 19. All models plotted together at severe surface roughness.

All of the other models and one of the two single habits plotted alongside C5 produce results similar to Fig. 17. Fig. 18 shows all the models and single habits at $D_{eff} = 50$ μm for moderate surface roughness, and Fig. 19 shows severe surface roughness. C5 is the same in both plots because that model does not consider surface roughness, except for the aggregate of columns which is severely roughened. Comparing the two plots, severe roughness has polarization values that are too low for all models, especially for scattering angles between $60°$ and $120°$, and the hollow column seems to fit very well, at least at this effective size. Fig. 20 shows the scattering phase matrix for hollow columns at moderate and severe surface roughness levels. Notice that for severely roughened crystals the $-P_{12}/P_{11}$ element is reduced in magnitude by almost half, leading to the polarization values that are too low to match the PARASOL data.

The result for hollow columns agrees with Labonnote et al. [49] and Baran et al. [48] who found that the Inhomogeneous Hexagonal Monocrystal model fit the POLDER (similar to newer PARASOL) polarized reflectance measurements the best out of the shapes they tried. IHM crystals are hexagonal columns which have random air bubble inclusions inside which serve to smooth out the phase matrix. More results for the hollow column will be examined in a later section.

It is not clear at this point which model is the best, since size dependence has not been examined. A conclusion can be made that moderate surface roughness is better than severe surface roughness overall for matching the PARASOL data from August 1, 2007. Next, the ice models will be examined at different effective diameters.
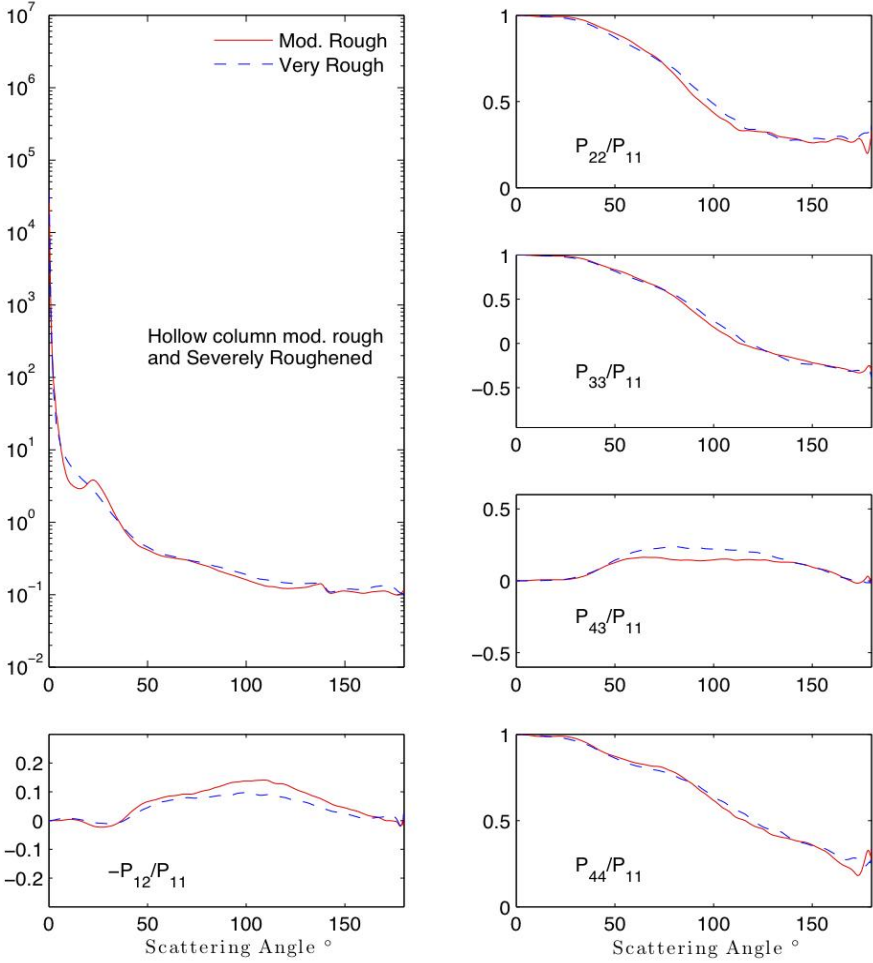
Fig. 20. Scattering phase matrix for hollow columns. Roughness is at moderate and severe levels.

Case 3

As in Case 2, the adding-doubling method is used to simulate the top of atmosphere Stokes vector and the polarized reflectance is obtained. The optical depth is again 1, and the wavelength is 0.865 μm. Fig. 21 shows the General model 1 ice model for all effective sizes at moderate roughness, and Fig. 22 shows the same model at all sizes for severe roughness. As seen before, the severely rough model is lower than measurements for all sizes except in this case for 10 μm, but at that size even severe roughness is too high, and the slope of the data in the scattering angle range from $60°$ to $90°$ is wrong. However, at large scattering angles from $130°$ or $140°$ to $180°$ severe roughness can actually provide a better fit in some cases. Overall, moderate roughness will provide a better fit, so all following plots will only consider moderately roughened ice crystals.

It is easiest to decipher the size dependence by looking at the lower end of the range of scattering angles, where Fig. 21 shows that there is a general decreasing trend in the polarized reflectance with increasing size, except for the largest size at $D_{eff} = 90$ μm, which increases slightly to provide a reasonable fit to the measurements. Figs. 23 through 28 show the size dependence of the rest of the ice models, along with solid and hollow columns.
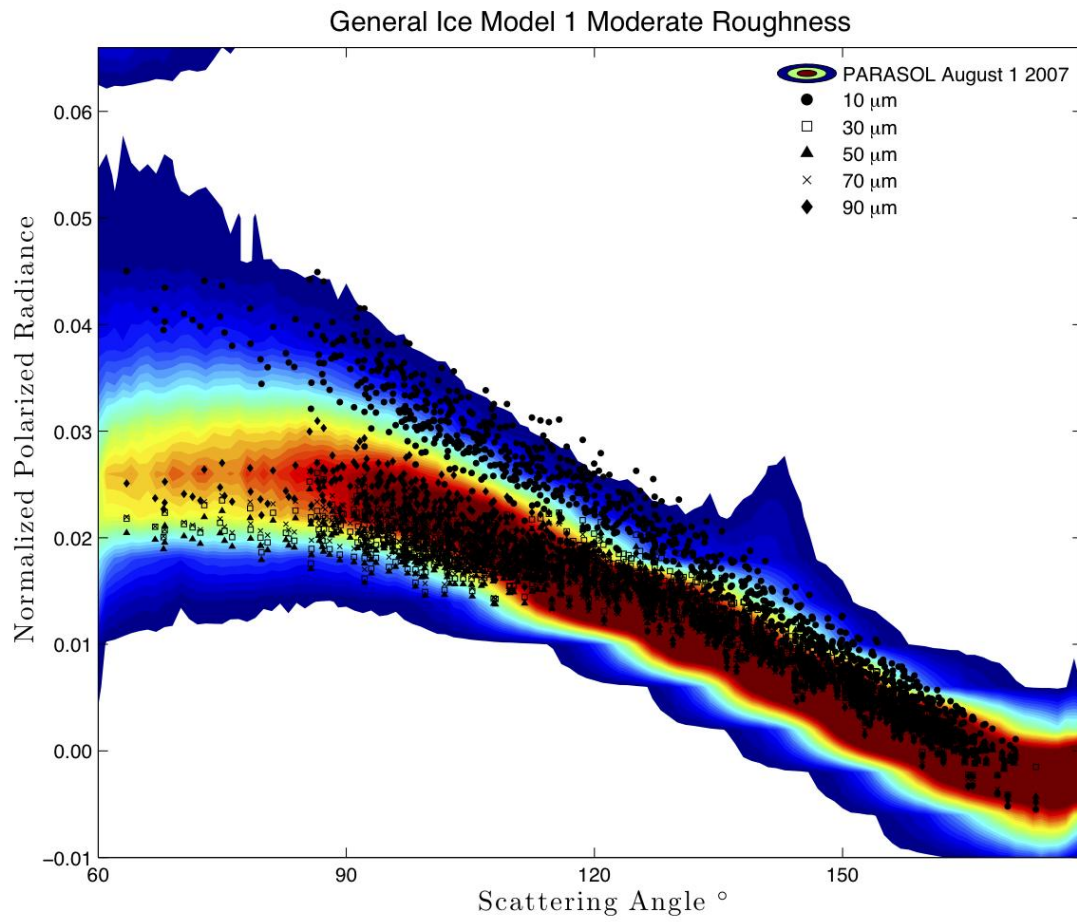
Fig. 21. General ice model 1 at all D_{eff} values for moderate roughness.
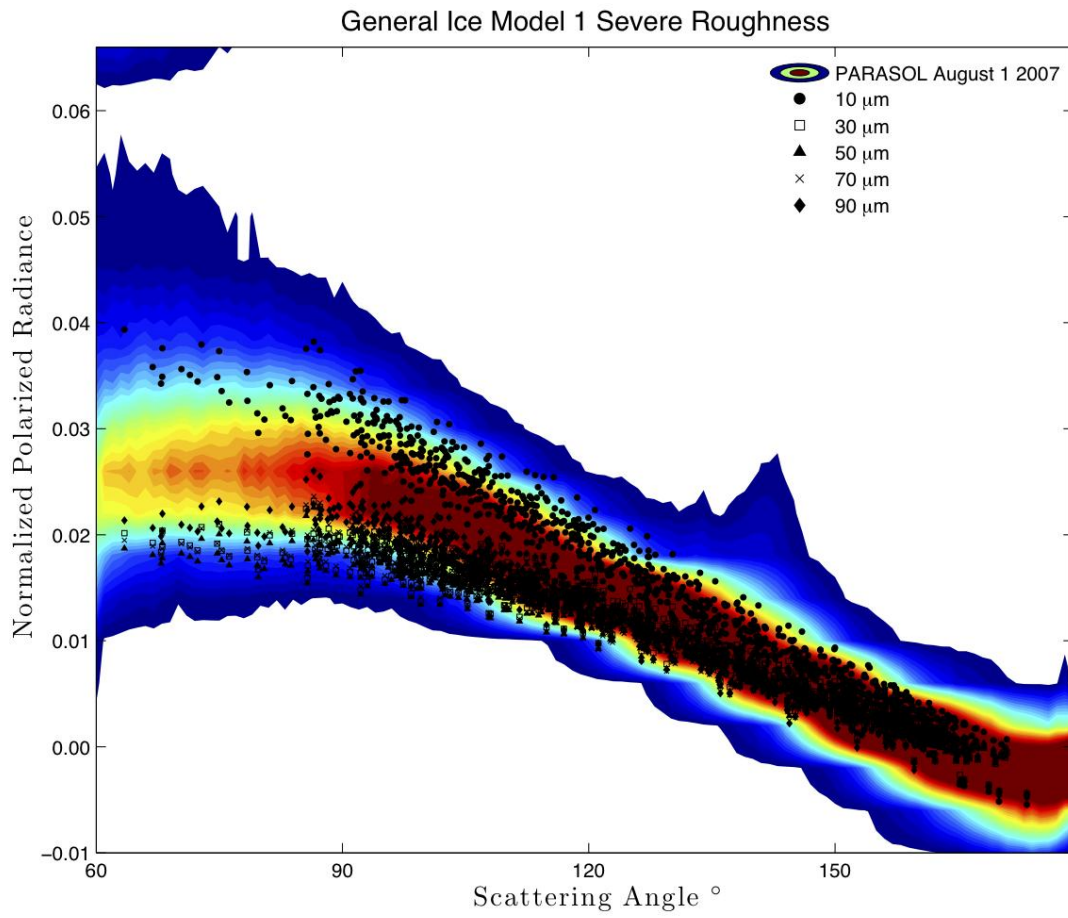
Fig. 22. General ice model 1 at all D_{eff} values for severe roughness.
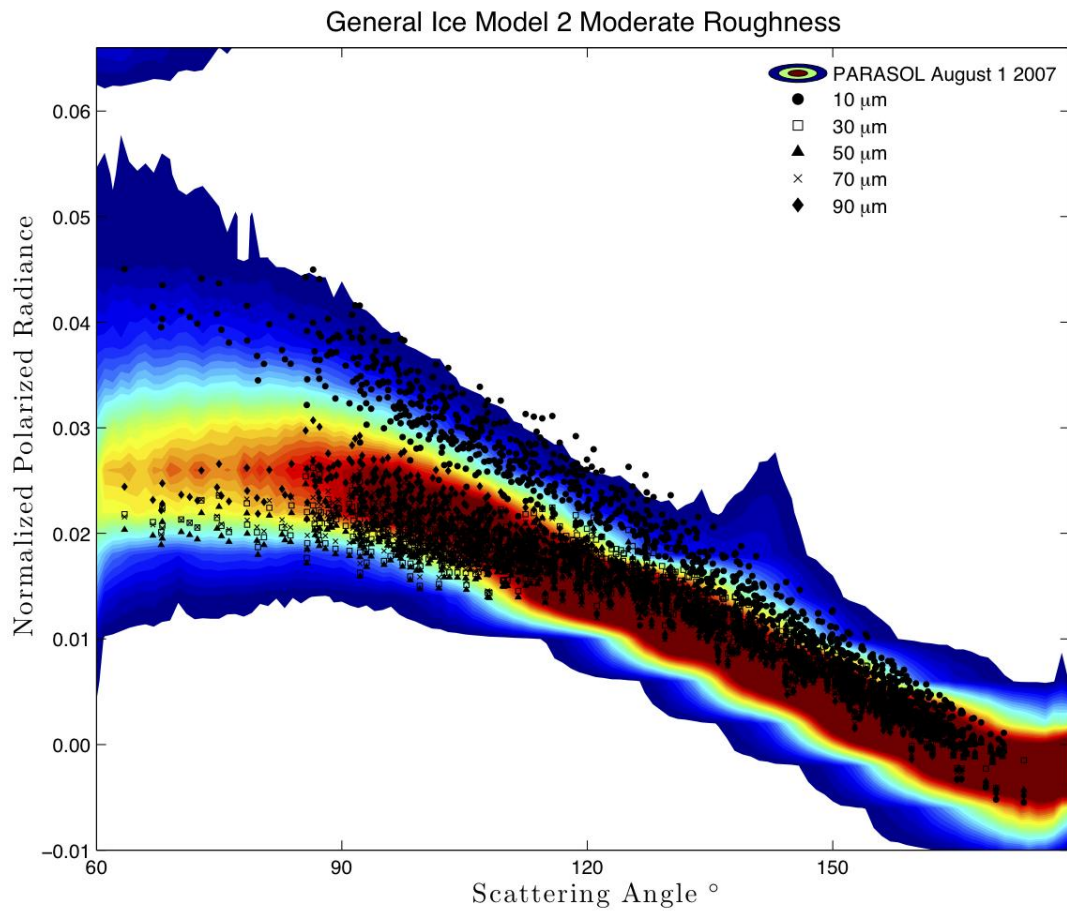
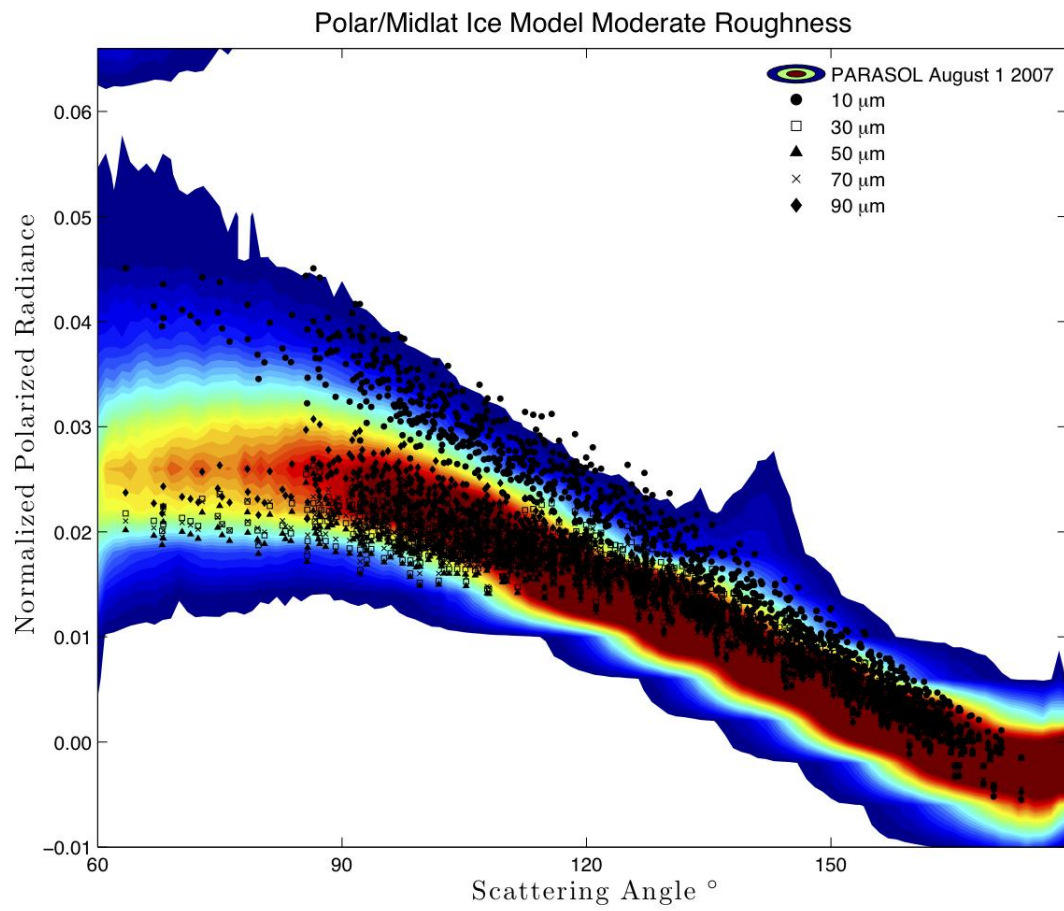Fig. 23. General ice model 2 at all sizes, moderate roughness.

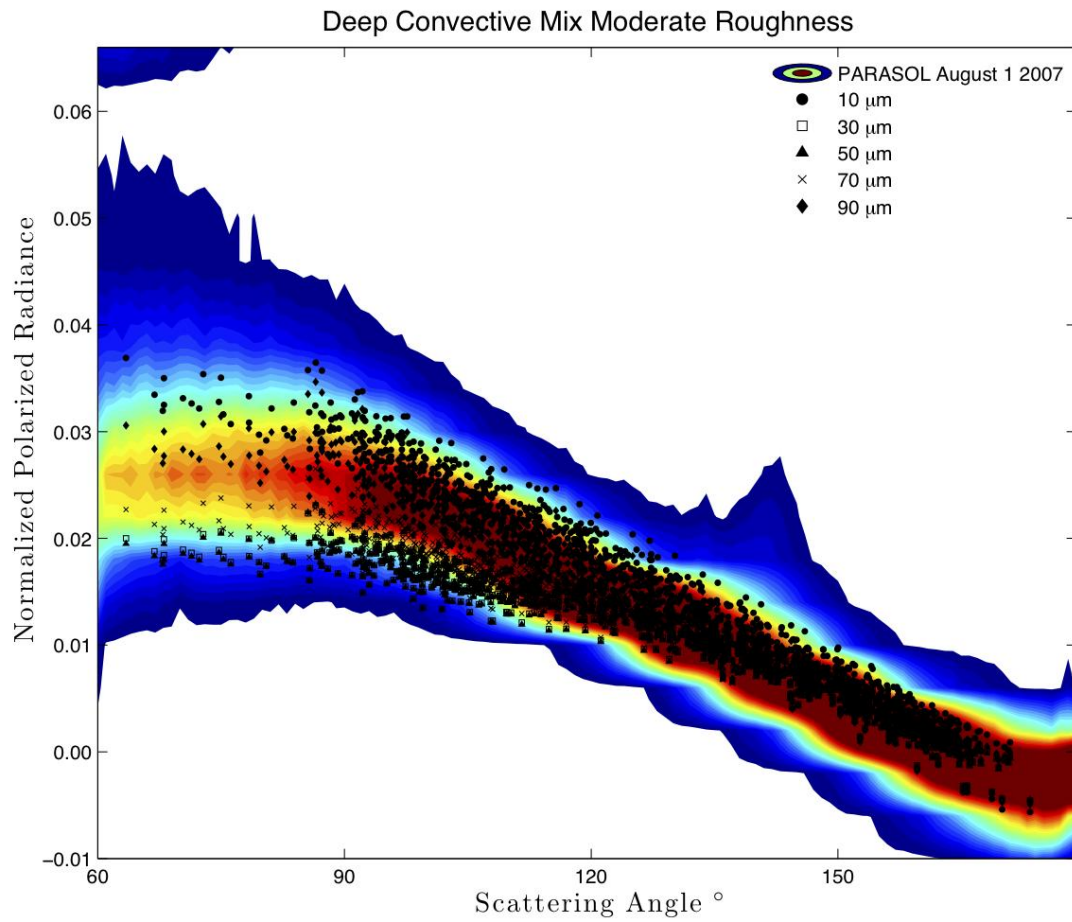Fig. 24. Polar/Mid-latitude model at all sizes, moderate roughness.

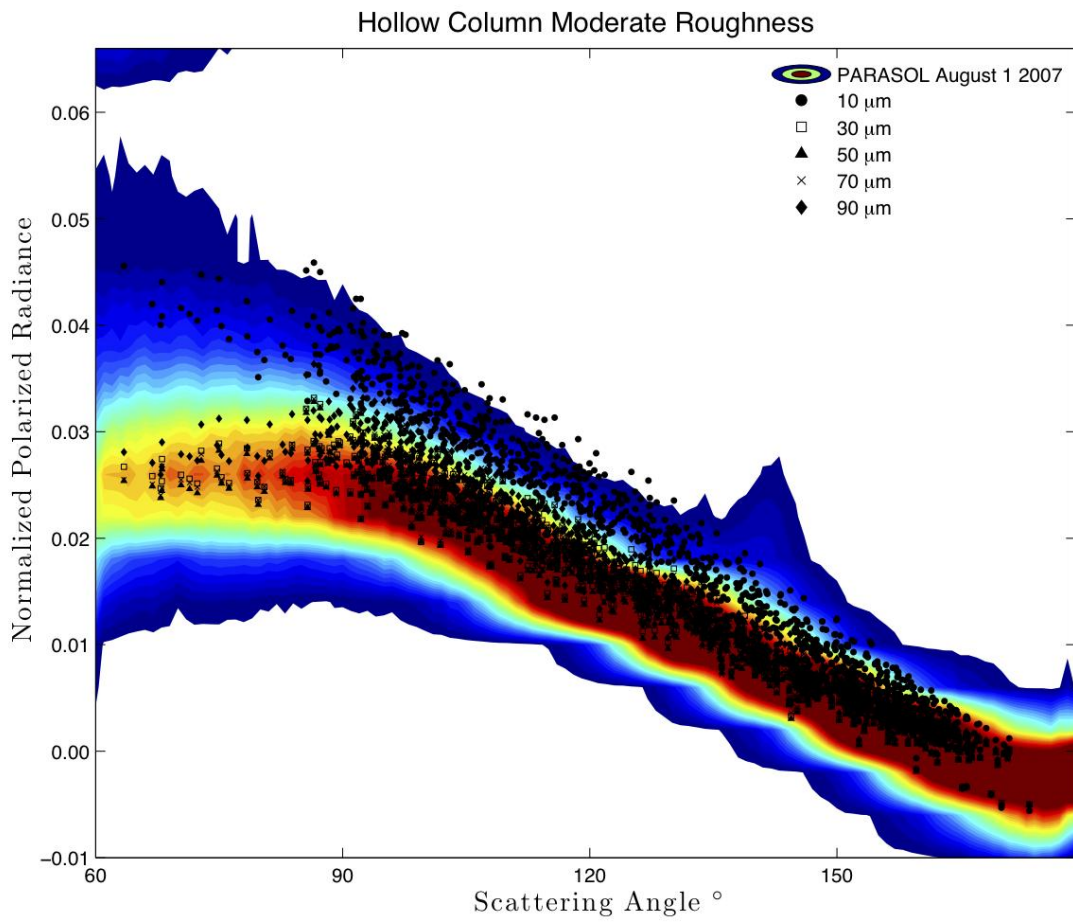Fig. 25. Deep convective ice model at all sizes, moderate roughness.

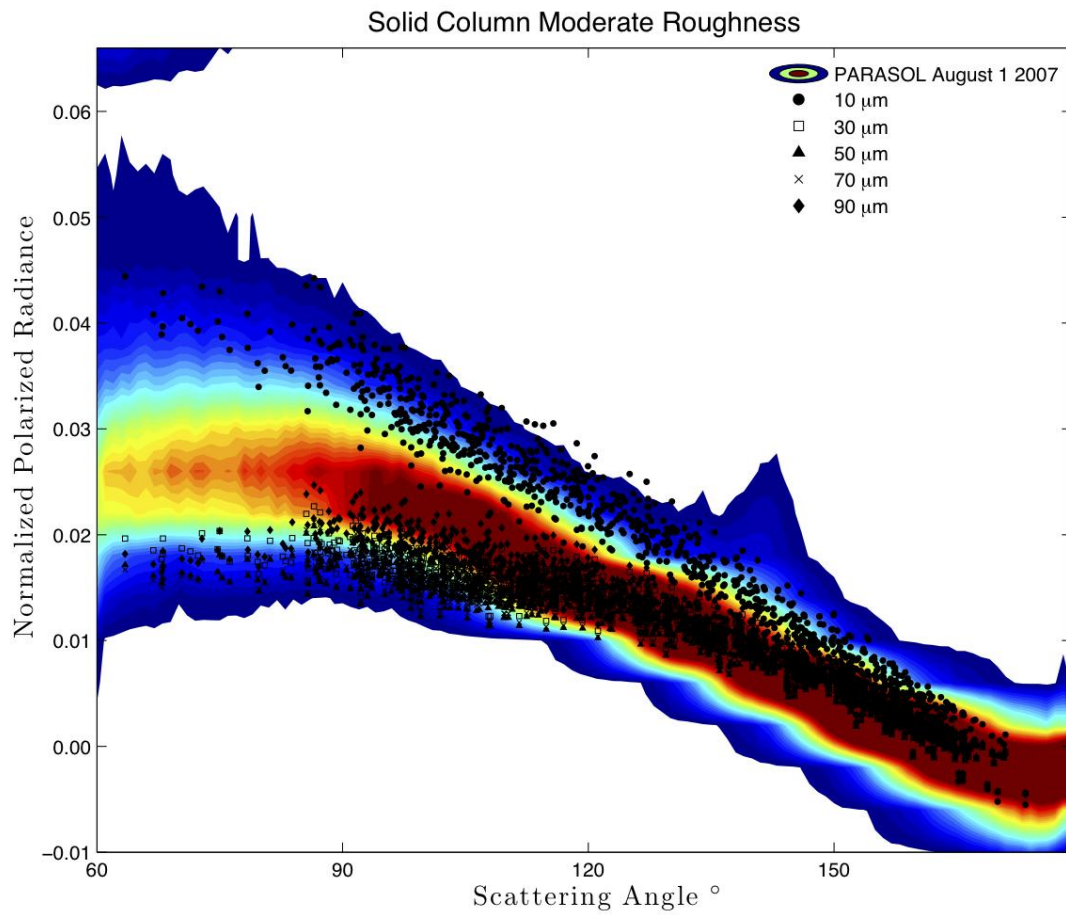Fig. 26. Hollow columns all sizes, moderate roughness.

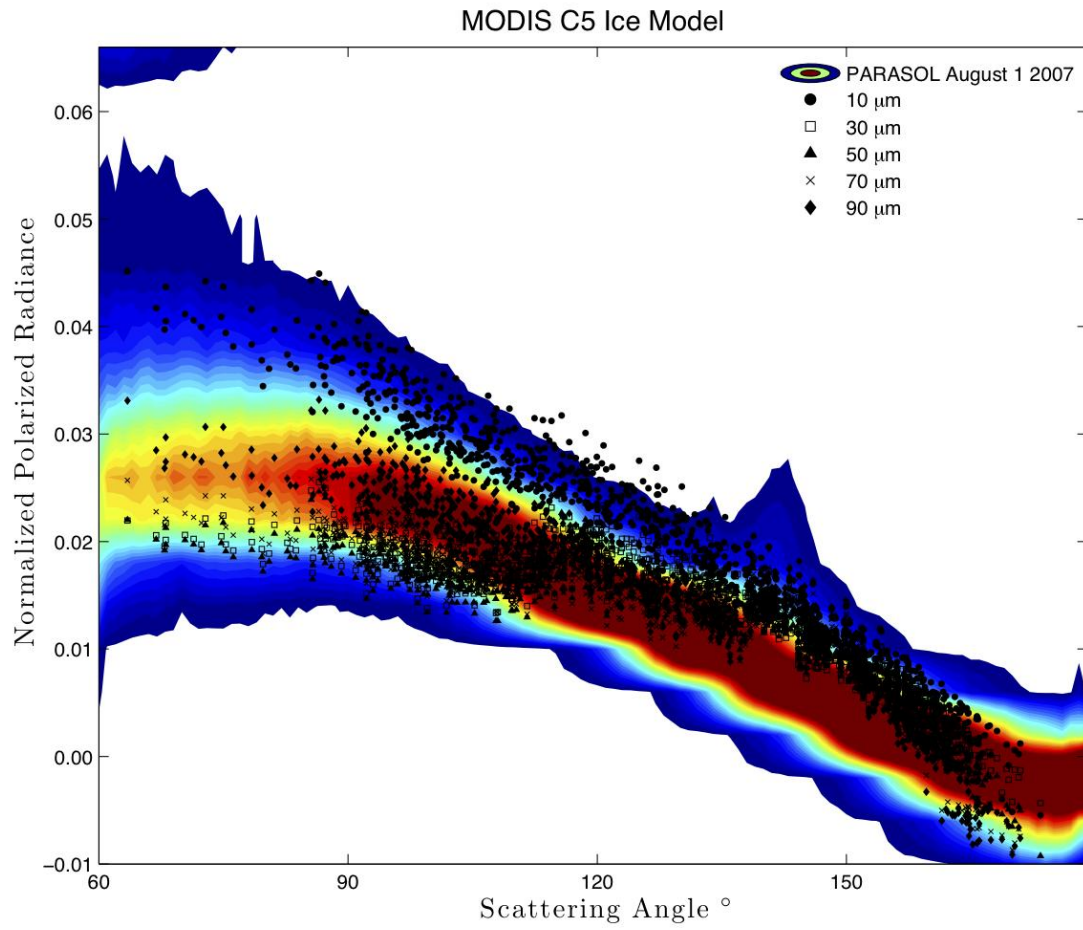Fig. 27. Solid columns at all sizes, moderate roughness.

Fig. 28. MODIS C5 model at all sizes, moderate roughness.

Looking over all the plots from Figs. 23 to 28, the same general trend of decreasing polarized reflectance with increasing size can be seen, with the largest size increasing slightly. Solid columns depart from the trend, failing to fit the measurements for any size. Hollow columns fit well at all sizes except for the smallest, while MODIS C5 does not have the correct negative slope of polarization with increasing scattering angle. Labonnote [49] also tested and rejected a model that also had the wrong slope of polarization (increasing near 140°) and a model that had values much too high at small scattering angles from 60° to 90°. Next, the best models will be chosen and compared.

Case 4

Based on the results from the previous cases, four models are examined in detail to find which one might provide the best match to the PARASOL data considered here. Figs. 29 to 32 show each of the four models plotted by itself against the polarized reflectance satellite data. Each one falls within the region where the greatest concentration of PARASOL data is located, hollow columns appear to be the best fit. As noted earlier, the hollow column is very similar to the IHM model proposed by Labonnote et al. [49] and Baran and Labonnote [48], which they found to provide a good fit to polarization measurements, so it is not surprising that the hollow column provides a good fit. The problem with the hollow column as a model is that while it may satisfy the polarization measurements, it has been shown that an ensemble of crystals more accurately represents ice water content (IWC) and median mass diameter [46].

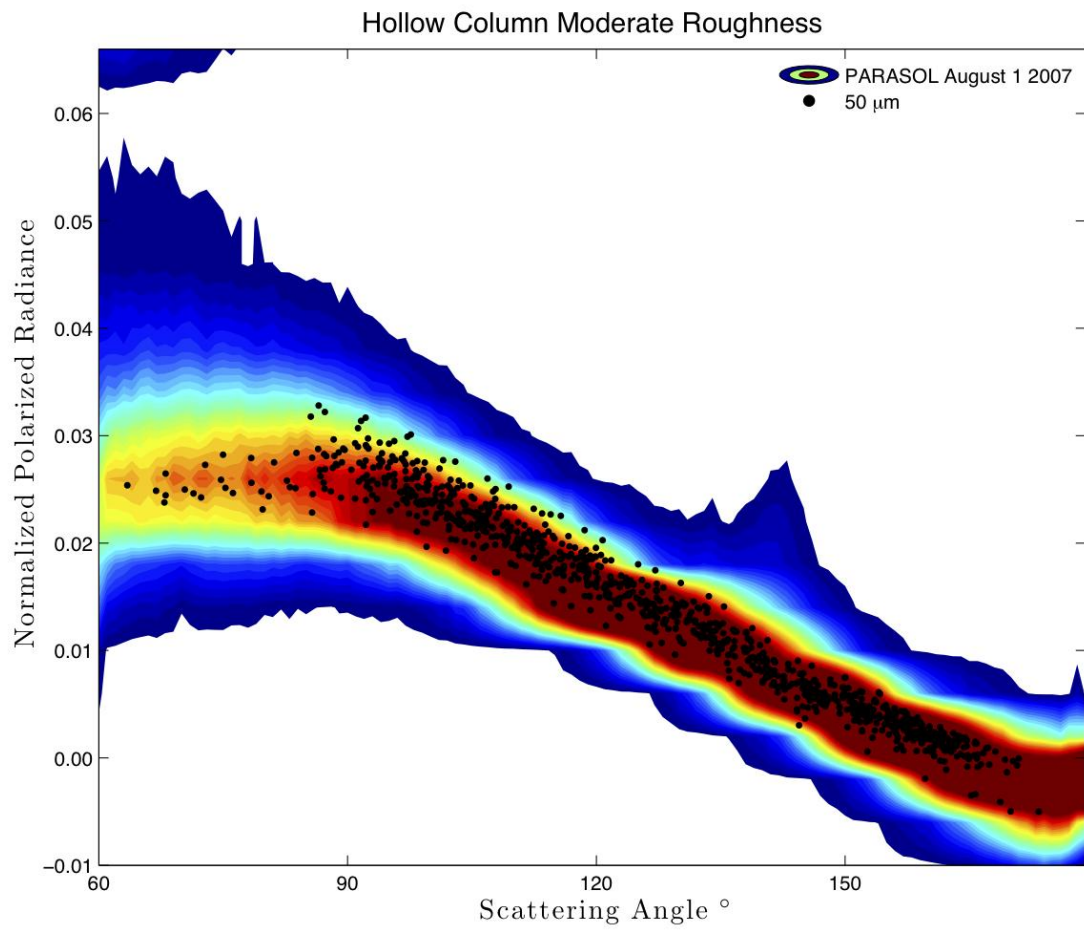Fig. 29. Hollow columns at D_{eff} = 50 μm, moderate roughness.

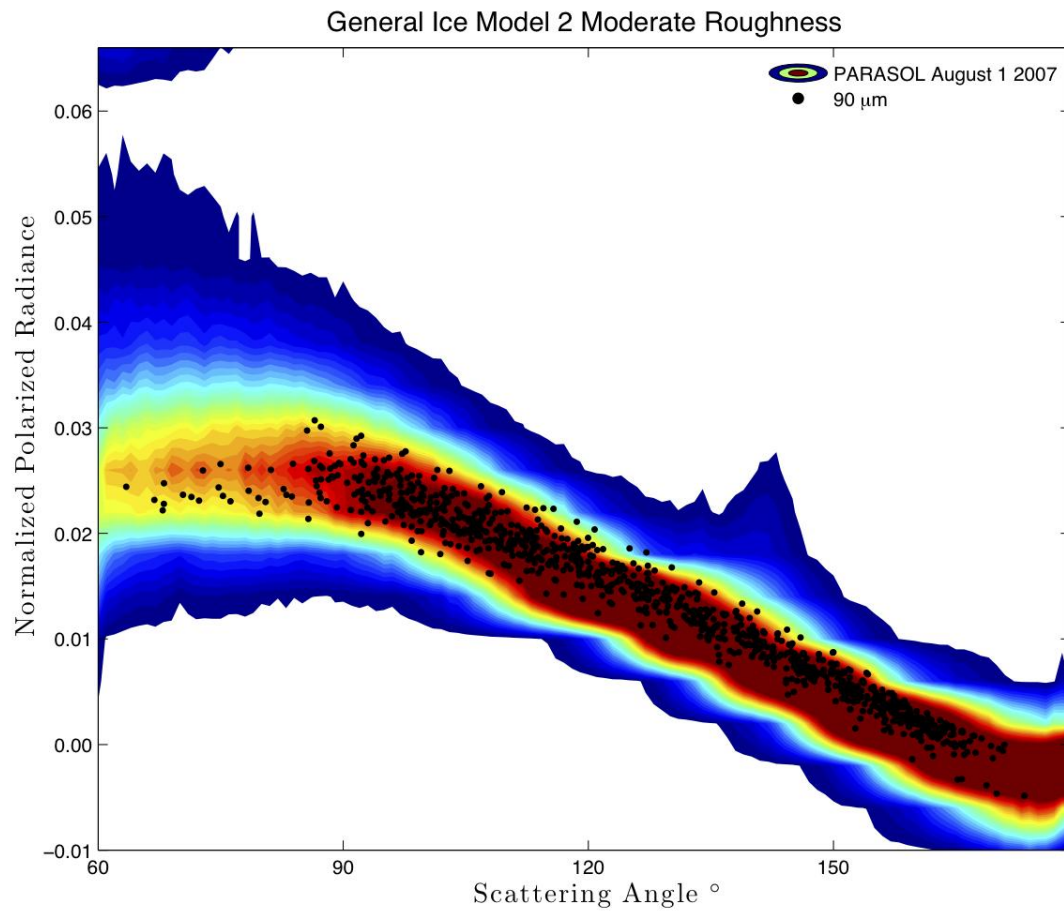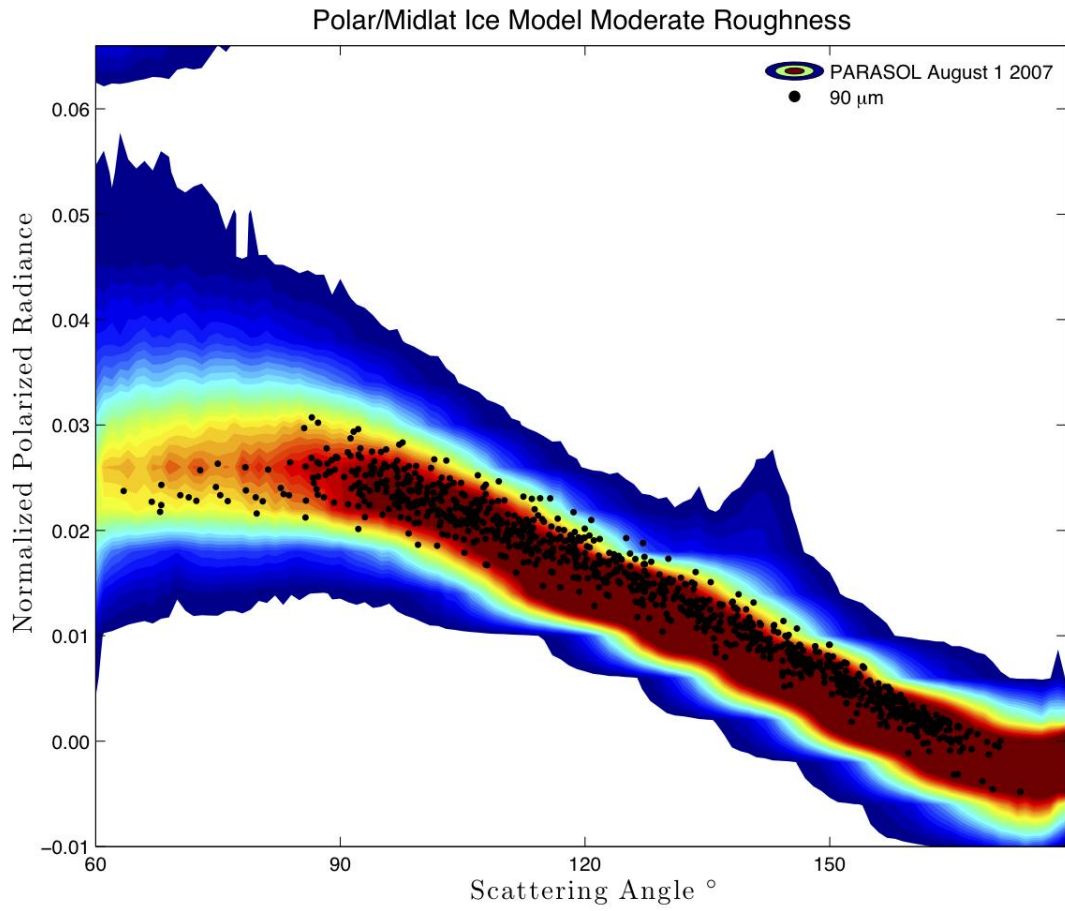Fig. 30. General model 2, moderate roughness, D_{eff} = 90 μm.

Fig. 31. Polar/Midlat model, moderate roughness, D_{eff} = 90 μm.
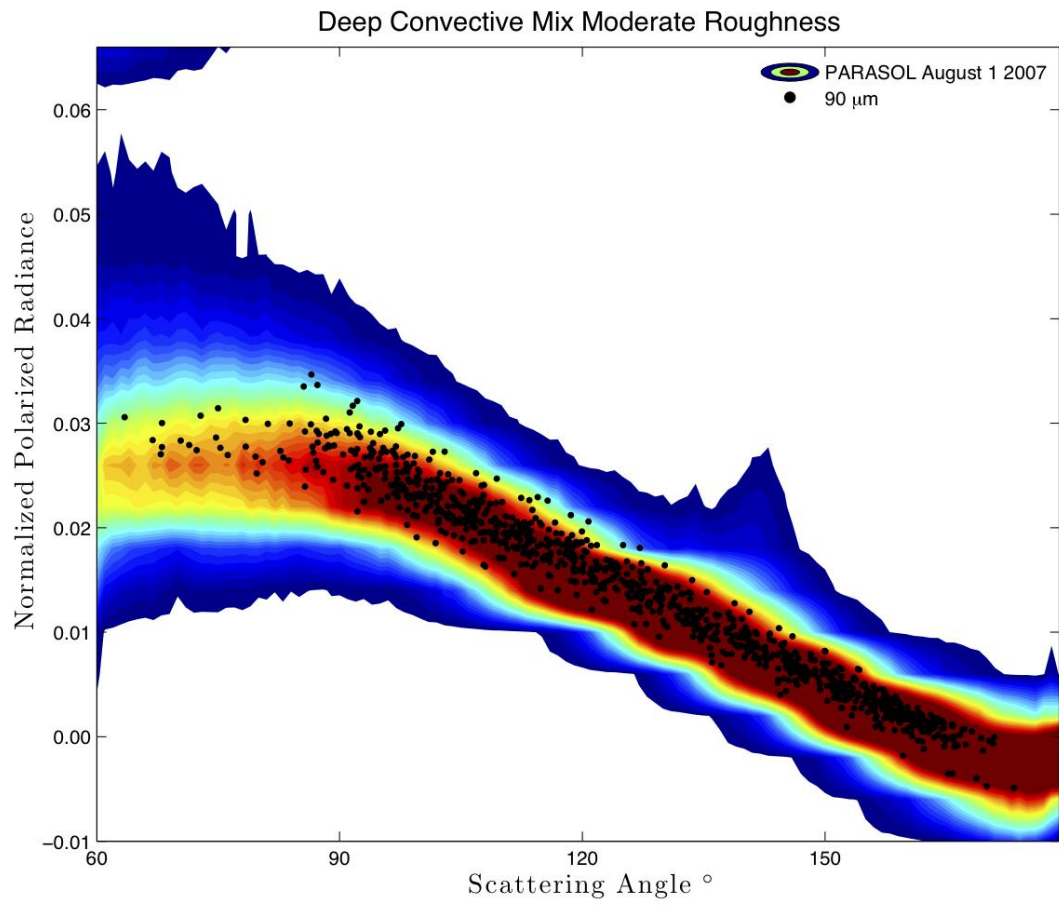
Fig. 32. Deep convective model, moderate roughness, $D_{eff} = 90$ μm.

Baran and Labonnote [57] use an ensemble approach in a subsequent paper to the IHM, one, clearly pointing out that the IHM model does not realistically represent IWC and median mass diameter and so should not be used to retrieve ice cloud properties on a global scale. Therefore, one of the models in the current study with an ensemble distribution of ice crystal shapes is likely better than hollow columns for remote sensing.

The reason that different ice models could closely match polarization data is that the PARASOL data contains many different types of ice cloudy pixels, including deep convective cirrus, mid-latitude synoptic cirrus, and polar cirrus, so each model will match some pixels very well and some not so well. A better way to approach the problem might be to detect pixels where cirrus from deep convection is located, and test the deep convective model on that data, and likewise for the other models. Previous ice cloud microphysical models have focused on global application of one model to all cirrus clouds no matter their source, but this approach may need to be modified.

One of the criteria for selecting PARASOL pixels was that it had a difference between minimum and maximum scattering angles in the pixel considered of at least 50°, which means many of the pixels considered in this study are in the midlatitudes because of the geometry involved. The mid-latitudes have more synoptically generated cirrus compared to deep convective cirrus, so the best overall model considered in this study is likely the polar/midlatitude ice model at a D_{eff} of 90 μm and moderate surface roughness.

To understand what scattering phase matrix features lead to modeled polarized reflectance which falls within the range of highest density of PARASOL measurements, the scattering phase matrix may be examined.
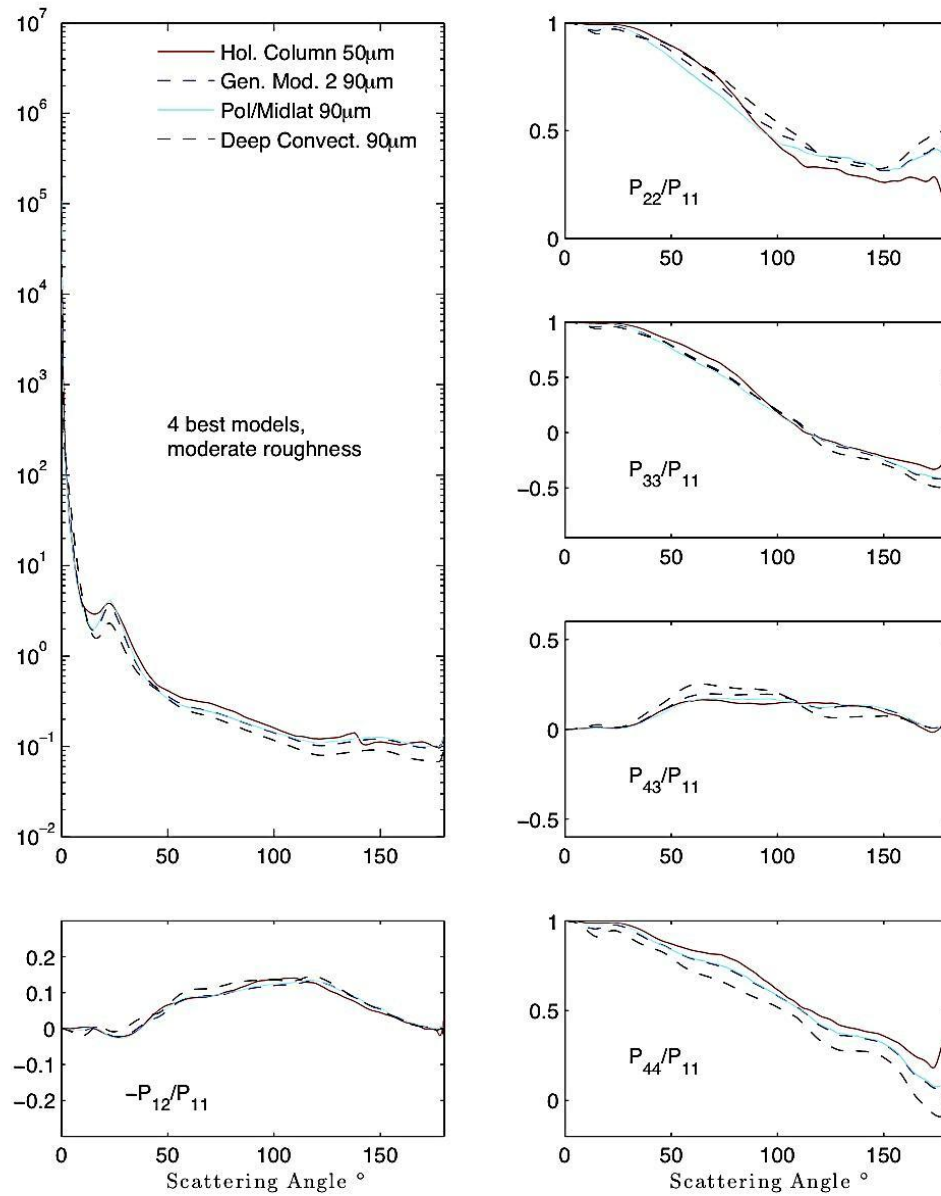
Fig. 33. Scattering phase matrix of the best models.
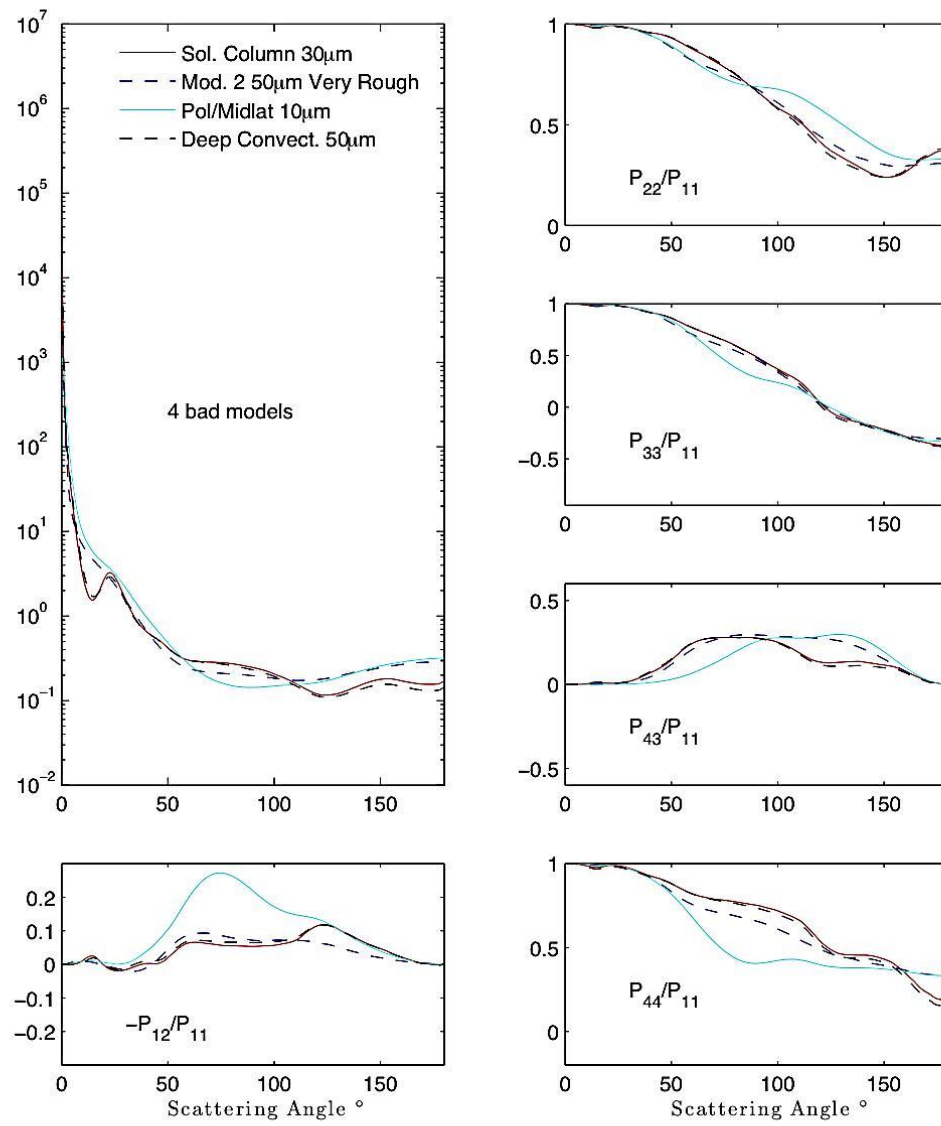
Fig. 34. Scattering phase matrix of the bad models.

The scattering phase matrix of the best models (modeled data falling within this highest density range) is shown in Fig. 33, and the scattering phase matrix for the worst models (furthest from the highest density range) is shown in Fig. 34. As expected, the $-P_{12}/P_{11}$ element for the good models is all nearly the same, reaching a maximum value of about 0.15 in a broad peak. The other scattering phase matrix elements from P_{11} to P_{44} are also close together and have the same trend in their slope, suggesting that the good models that assume different habit and size distributions all end up with similar scattering properties.

Considering the bad models now, $-P_{12}/P_{11}$ is not the same shape for all the models. Some have values that are higher or lower than the good models, the same trend which was seen in the polarized reflectance plots. All good models in this study have the halo angle of $22°$ (caused by radiation traveling through two side facets of a hexagonal column crystal) present in the phase function P_{11}, but some bad models have it and some do not. Combined with the fact that hollow columns matched the PARASOL polarized reflectance the best, hollow columns seem to be one of the components of an ice microphysical model needed in order to match the observed polarization.

CHAPTER VIII

DISCUSSION AND SUMMARY

An adding-doubling method was used to calculate the TOA Stokes vector for the case of a thin cirrus cloud at the solar wavelength of 0.865 μm, and the effective Mueller matrix and polarized reflectance were calculated from it. The effective Mueller matrix was studied as a way to distinguish between habit distributions, and polarized reflectance data from the PARASOL satellite was used to compare with modeled data to determine the habit distribution and surface roughness which best fit the measurements.

For the effective Mueller matrices in case 1, it was not possible to distinguish between the different habit distributions, except in the case of the deep convective model where the M_{14}/M_{11} element showed a large difference from the C5 model. This difference is most likely due to multiple scattering in the many branches of the large crystals that make up the majority of the habit distribution for the deep convective model. The linear polarization is also lower for the deep convective model, again likely due to multiple scattering.

For case 2, the MODIS Collection 5 ice microphysical model was tested against several different ice models at different levels of surface roughness. The C5 model has a peak near $150°$ that is not seen in the satellite data, and also has the wrong slope of polarization. The C5 model does not consider surface roughness except for the aggregate of columns, and as such its phase matrix still contains many sharp features that lead to poor agreement with remote sensing measurements [57]. The level of surface roughness

that best fits the PARASOL data seems to be moderate roughness, although for some sizes severe roughness gives a good fit at large scattering angles from $120°$ to $180°$. Severe roughness does not fit at small scattering angles for any size. Moderate roughness eliminates many phase function features such as the $46°$ halo and reduces the sharpness of others without reducing the $-P_{12}/P_{11}$ element too much, while severe roughness eliminates the $22°$ and $46°$ halos and the $180°$ backscatter peak and also reduces $-P_{12}/P_{11}$ too far.

Case 3 compared the ice models at different effective diameters to investigate the size dependence of polarized reflectance. In all cases, the smallest effective diameter had the largest polarization values, much higher than the measurements. There was a general decreasing trend with size until the largest size, which increased slightly in polarization. Solid columns did not fit the measurements at any size, whereas hollow columns fit the measurements at every size except the smallest, 10 μm. The MODIS C5 model did not fit the polarization values or decreasing trend with scattering angle at any effective size and generally had values that were too high.

Case 4 compared four models that were selected from the earlier comparisons as the best fits to decide which one was the best match to the one day of PARASOL data considered. While the hollow column was the closest match for polarization, it is not the best for an ice model to use in remote sensing because many authors have found that the IWC, median mass diameter, and other parameters are not accurate with a single-habit model [46,57]. Ensemble models can provide reasonable values for the IWC and also match well with polarization. The polar/mid-latitude model in this study largely

followed the PARASOL polarization values, and it is likely that with an algorithm to select pixels of a certain type of cirrus, whether synoptic mid-latitude, deep convective, or other, that the match of an ensemble model with measurement will become very good. The data presented here do not discriminate between different types of ice cloudy pixels and so the model must match all different types of microphysics with one habit mixture.

The scattering phase matrix of the four best models was very similar, especially in the $-P_{12}/P_{11}$ element. The maximum value was about 0.15 occurring in a broad peak around the scattering angle of $100°$. Each model also had a discernible $22°$ halo in the phase function, meaning that hexagonal crystals of some type are present in ice clouds. Hollow columns fit the polarization the best in this study, so it is likely that this habit occurs in relative abundance in ice clouds. All ensemble ice models should include a fraction of this type of crystal in order to match polarization measurements and accurately model ice clouds.

Polarization is a powerful tool to select the best ice model for use in simulating the optical and microphysical properties of ice clouds. Ensemble ice models for use in global studies should be compared with polarized reflectance from PARASOL or another polarization instrument to make sure the model accurately reflects reality. The present study indicates that the current MODIS C5 model does not match observed polarized reflectance from PARASOL, and therefore is not a good model. Three ensemble ice models in this study, each with moderately roughened crystals and an effective diameter D_{eff} of 90 μm, match the polarized reflectance values reasonably well

and are good candidates for use in remote sensing of cirrus clouds and simulation of

cirrus clouds in global climate models.

REFERENCES

1. J.M. Edwards, S. Havemann, J-C Thelen, and A.J. Baran, "A new parametrization for the radiative properties of ice crystals: comparison with existing schemes and impact in a GCM," Atmos. Res. **83**, 19-35 (2007).

2. K. Sassen, Z. Wang, and D. Liu, "Global distribution of cirrus clouds from the CloudSat/Cloud-Aerosol Lidar and Infrared Pathfinder Satellite Observations (CALIPSO) measurements," J. Geophys. Res. **113**, D00A12 (2008).

3. A.J. Baran, "A review of the light scattering properties of cirrus," J. Quant. Spec. Rad. Trans. **110**, 1239-1260 (2009).

4. Y.S. Choi and C. H. Ho, "Radiative effects of cirrus with different optical properties over the tropics in MODIS and CERES observations," Geophys. Res. Lett. **33**, L21811 (2006).

5. H. Nazaryan, M.P. McCormick, and W.P. Menzel, "Global characterization of cirrus clouds using CALIPSO data," J. Geophys. Res. **113**, D16211 (2008).

6. A.J. Heymsfield, A. Bansemer, P.R. Field, S.L. Durden, J.L. Stith, J.E. Dye, et al., "Observations and parameterizations of particle size distributions in deep tropical cirrus and stratiform precipitating clouds: results from in situ observations in TRMM field campaigns," J. Atmo. Sci. **59**, 3457-3491 (2002).

7. A.J. Heymsfield and L.M. Miloshevich, "Relative humidity and temperature influences on cirrus formation and evolution: observations from wave clouds and FIRE II," J. Atmos. Sci. **52**, 4302-4326 (1995).

8. Q. Fu, "A new parameterization of an asymmetry factor of cirrus clouds for climate models," J. Atmos. Sci. **64**, 4140-4150 (2007).

9. H. Chepfer, G. Brogniez, and Y. Fouquart, "Cirrus clouds' microphysical properties deduced from POLDER observations," J. Quant. Spec. Rad. Trans. **60**, 375-390 (1998).

10. B.A. Baum, P. Yang, Y.X. Hu, and Q. Feng, "The impact of ice particle roughness on the scattering phase matrix," J. Quant. Spec. Rad. Trans. **111**, 2534-2549 (2010).

11. J.F. de Haan, P.B. Bosma, and J.W. Hovenier, "The adding method for multiple scattering calculations of polarized light," Astron. Astrophys. **183**, 371-391 (1987).

12. G.M. McFarquhar and A.J. Heymsfield, "Microphysical characteristics of three anvils sampled during the central equatorial Pacific experiment," J. Atmos. Sci. **53**, 2401-2423 (1996).

13. K.N. Liou, *An Introduction to Atmospheric Radiation* (Academic Press, 2002).

14. L. Bi, P. Yang, G. Kattawar, B.A. Baum, Y.X. Hu, and J.Q. Lu, "Simulation of the color ratio associated with the backscattering of radiation by ice crystals at 0.532 and 1.064-μm wavelengths," J. Geophys. Res. **114**, D00H08 (2009).

15. Y. Takano and K.N. Liou, "Solar radiative transfer in cirrus clouds. part I: single-scattering and optical properties of hexagonal ice crystals," J. Atmos. Sci. **46**, 3-19 (1989).

16. Q. Cai and K.N. Liou, "Polarized light scattering by hexagonal ice crystals: theory," Appl. Optics **21**, 3569-3580 (1982).

17. P. Yang and K.N. Liou, "Light scattering by hexagonal ice crystals: comparison of finite-difference time domain and geometric optics models," J. Opt. Soc. Amer. A **12**, 162-176 (1995).

18. P. Yang, G.W. Kattawar, G. Hong, P. Minnis, and Y. Hu, "Uncertainties associated with the surface texture of ice particles in satellite-based retrieval of cirrus clouds: part I. single scattering properties of ice crystals with surface roughness," IEEE Trans. Geosci. Rem. Sens. **46**, 1940-1947 (2008).

19. B.A. Baum, P. Yang, A.J. Heymsfield, C.G. Schmitt, Y. Xie, A. Bansemer, Y.X. Hu, and Z. Zhang, "Improvements in shortwave bulk scattering and absorption models for the remote sensing of ice clouds," J. Appl. Met. Clim. **50**, 1037-1056 (2011).

20. J.D. Jackson, *Classical Electrodynamics*, 3rd ed. (John Wiley and Sons, 1998).

21. S. Chandrasekhar, *Radiative Transfer* (Dover, 1960).

22. H.C. van de Hulst, *Light Scattering by Small Particles* (John Wiley and Sons, 1957).

23. G.G. Stokes, "On the composition and resolution of streams of polarized light from different sources," in *Polarized Light*, W. Swindell, ed. (Dowden, Hutchinson & Ross, 1975), pp. 124-141.

24. S. Chandrasekhar, "On the radiative equilibrium of a stellar atmosphere. XV," Astrophys. J. **105**, 424 (1947).

25. G.N. Plass and G.W. Kattawar, "Monte Carlo calculations of light scattering from clouds," Applied Optics **7**, 415-419 (1968).

26. L. Di Girolamo, L. Liang, and S.E. Platnick, " A global perspective on the plane-parallel nature of oceanic clouds," Geophys. Res. Lett. **37**, doi:10/.1029/2010GL044094 (2010).

27. F.M. Breon, *Parasol Level-1 Product Data Format and User Manual*, Ed. 1, Rev. 3 (CNES, April 13th, 2006).

28. P. Deschamps, F.M. Breon, M. Leroy, A. Podaire, A. Bricaud, J.C. Buriez, and G. Seze, "The POLDER mission: instrument characteristics and scientific objectives," IEEE Trans. Geosci. Rem. Sensing **32**, 598-615 (1994).

29. F.M. Breon, *Parasol Level-2 Product Data Format and User Manual*, Ed. 1, Rev. 3 (CNES, Nov. 12th, 2009).

30. H.C. van de Hulst, *Multiple Light Scattering: Tables, Formulas, and Applications* Vol. I (Academic Press, 1980).

31. H.H. Tynes, *Monte Carlo Solutions of the Radiative Transfer Equation for Scattering Systems* [Dissertation] (Texas A&M University, College Station, TX, 2001).

32. C.N. Adams and G.W. Kattawar, "Effect of volume-scattering function on the errors induced when polarization is neglected in radiance calculations in an atmosphere-ocean system," Applied Optics **32** (24), 4610-4617 (1993).

33. R.L. Lawless, *Sensitivity of the Mueller Matrix to the Optical and Microphysical Properties of Cirrus Clouds* [Thesis] (Texas A&M University, College Station, TX, 2005).

34. E. Hecht, *Optics*, 4th ed. (Addison Wesley, 2002).

35. C.F. Bohren and D.R. Huffman, *Absorption and Scattering of Light by Small Particles* (Wiley Interscience, 1983).

36. J.W. Hovenier, C. Van der Mee, and H. Domke, *Transfer of Polarized Light in Planetary Atmospheres* (Kluwer Academic Publishers, 2004).

37. H. Mueller, "The foundations of optics," J. Opt. Soc. Am. **38**, 661 (1948).

38. A.H. Hielscher, A.A. Eick, J.R. Mourant, D. Shen, J.P. Freyer, and I.J. Bigio, "Diffuse backscattering Mueller matrices of highly scattering media," J. Opt. Soc. Am. **1**, 441-453 (1997).

39. R. Lawless, Y. Xie, P. Yang, G.W. Kattawar, and I. Laszlo, "Polarization and effective Mueller matrix for multiple scattering of light by nonspherical ice crystals," Optics Express **14,** 6381-6393 (2006).

40. H.H. Tynes, G.W. Kattawar, E.P. Zege, I.L. Katsev, A.S. Prikhach et al., "Monte Carlo and multicomponent approximation methods for vector radiative transfer by use of effective Mueller matrix calculations," Appl. Optics **40** (3), 400-412 (2001).

41. R.W. Ditchburn, *Light* (Dover, 1991).

42. P Yang and K.N. Liou, "Geometric-optics-integral-equation method for light scattering by nonspherical ice crystals," Applied Optics **35**, 6568-6584 (1996).

43. P. Yang and K.N. Liou, "Light scattering by hexagonal ice crystals: solutions by a ray-by-ray integration algorithm," J. Opt. Soc. Am. A **14**, 2278-2289 (1997).

44. G.G. Mace, E.E. Clothiaux, and T.P. Ackerman, "The composite characteristics of cirrus clouds: bulk properties revealed by one year of continuous cloud radar data," J. Climate **14**, 2285-2303 (2001).

45. B.A. Baum, P. Yang, A.J. Heymsfield, S. Platnick, M.D. King, Y.X. Hu, and S.T. Bedka, "Bulk scattering properties for the remote sensing of ice clouds. part II: narrowband models," J. Appl. Met. **44**, 1896-1911 (2005).

46. B.A. Baum, A.J. Heymsfield, P. Yang, and S.T. Bedka, "Bulk scattering properties for the remote sensing of ice clouds. part I: microphysical data and models," J. Appl. Met. **44**, 1885-1895 (2005).

47. A.J. Baran and S. Havemann, "The dependence of retrieved cirrus ice-crystal effective dimension on assumed ice-crystal geometry and size-distribution function at solar wavelengths," Q.J.R. Met. Soc. **130**, 2153-2167 (2004).

48. A.J. Baran and L.C. Labonnote, "On the reflection and polarization properties of ice cloud," J. Quant. Spec. Rad. Trans. **100**, 41-54 (2006).

49. L.C. Labonnote, G. Brogniez, J.C. Buriez, and M. Doutriaux-Boucher, "Polarized light scattering by inhomogeneous hexagonal monocrystals: Validation with ADEOS-POLDER measurements," J. Geophys. Res. **106**, 12,139-12,153 (2001).

50. G.P. Anderson, J.H. Chetwynd, S.A. Clough, E.P. Shettle, and F.X. Kneizys, "AFGL atmospheric constituent profiles (0-120km)," Optical Physics Division report, Air Force Geophysics Laboratory, AFGL-TR-86-0110 (1986). Retrieved from http://www.dtic.mil/cgi-bin/GetTRDoc?Location=U2&doc=GetTRDoc.pdf&AD=ADA175173 on November 10, 2010.

51. A.T. Young, "Revised depolarization corrections for atmospheric extinction," Appl. Optics **19**, 3427-3428 (1980).

52. C. Tomasi, V. Vitale, B. Petkov, A. Lupi, and A. Cacciari, "Improved algorithm for calculations of Rayleigh-scattering optical depth in standard atmospheres," Appl. Optics **44**, 3320-3341 (2005).

53. W.J. Wiscombe, "The Delta-M method: rapid yet accurate radiative flux calculations for strongly asymmetric phase functions," J. Atmo. Sci. **34**, 1408-1422 (1977).

54. Y.X. Hu, B. Wielicki, B. Lin, G. Gibson, S.C. Tsay, K. Stamnes, and T. Wong, "δ-fit: a fast and accurate treatment of particle scattering phase functions with weighted singular-value decomposition least-squares fitting," J. Quant. Spec. Rad. Trans. **65**, 681-690 (2000).

55. M. Chami, R. Santer, and E. Dilligeard, "Radiative transfer model for the computation of radiance and polarization in an ocean-atmosphere system: polarization properties of suspended matter for remote sensing," Applied Optics **40**, 2398-2416 (2001).

56. J.W. Hovenier and C.V.M. van der Mee, "Fundamental relationship relevant to the transfer of polarized light in a scattering atmosphere," Astron. Astrophy. **128**, 1-16 (1983).

57. A.J. Baran and L.C. Labonnote, "A self-consistent scattering model for cirrus. I: the solar region," Q. Jour. Royal Met. Soc. **133**, 1899-1912 (2007).

APPENDIX A

ICE MODEL HABIT PERCENTAGES

Table 3. MODIS C5 ice model habit percentages. Size is measured as the maximum dimension of each crystal.

Crystal Habit	< 0.006 cm	0.006 – 0.1 cm	0.1 – 0.25 cm	> 0.25 cm
Droxtal	100%	0	0	0
Solid bullet rosette	0	15%	0	97%
Plate	0	35%	0	0
Solid column	0	50%	45%	0
Hollow column	0	0	45%	0
Aggregate of columns	0	0	10%	3%

Table 4. Habit percentages for the mid-latitude ice cloud models. This table is for general model 1. General model 2 is exactly the same, except for in the second size range plates are only 20% and hollow columns are 45%.

Crystal Habit	< 0.001 cm	.001 – .015 cm	.015 – .05 cm	.05 – .075 cm	.075 - .1 cm	.1-.125 cm	>.125 cm
Droxtal	100%	Decrease to 0	0	0	0	0	0
Solid bullet rosette	0	0	Increase to 20%	Increase to 26.25%	Increase to 32.5%	32.5%	32.5%
Plate	0	Increase to 30%	Decrease to 0	0	0	0	0
Solid column	0	Increase to 35%	Decrease to 0	0	0	0	0
Hollow column	0	Increase to 35%	Decrease to 0	0		0	0
Aggregate of columns	0	0	Increase to 30%	Decrease to 17.5%	Decrease to 5%	5%	5%
Small aggregate of plates	0	0	Increase to 30%	Decrease to 26.25%	Decrease to 11.25%	Decrease to 0	0
Large aggregate of plates	0	0	0	0	Increase to 11.25%	Increase to 22.5%	22.5%
Hollow bullet rosettes	0	0	Increase to 20%	Increase to 30%	Increase to 40%	40%	40%

Table 5. Habit percentages for the polar/mid-latitude ice cloud model.

Crystal Habit	< .001 cm	.001 – .015 cm	.015 – .05 cm	.05 - .1 cm	>.1 cm
Droxtal	100%	0	0	0	0
Solid bullet rosette	0	Increase to 10%	Increase to 20%	Increase to 30%	30%
Hollow bullet rosette	0	Increase to 20%	Increase to 40%	Increase to 60%	60%
Solid column	0	Increase to 20%	Decrease to 10%	Decrease to 0	0
Hollow column	0	Increase to 30%	Decrease to 10%	Decrease to 0	0
Aggregate of columns	0	Increase to 10%	Increase to 20%	Decreases to 10%	10%
Small aggregate of plates	0	0	0	0	0
Large aggregate of plates	0	0	0	0	0
Plate	0	Increase to 10%	Decrease to 0	0	0

Table 6. Habit percentages for the deep convective ice cloud model.

| Crystal Habit	< .001 cm	.001 – .02cm	.02 – .075 cm	.075 - .125 cm	>.125 cm
Droxtal	0	0	0	0	0
Solid bullet rosette	0	0	Increase to 2%	Increase to 4%	4%
Hollow bullet rosette	0	0	Increase to 3%	Increase to 6%	6%
Solid column	100%	Decrease to 20%	Decrease to 0	Decrease to 0	0
Hollow column	0	Increase to 20%	Decrease to 0	Decrease to 0	0
Aggregate of columns	0	0	Increase to 15%	Decrease to 5%	5%
Small aggregate of plates	0	0	Increase to 70%	Decrease to 0%	0
Large aggregate of plates	0	0	0	Increase to 85%	85%
Plate	0	Increase to 60%	Decrease to 10%	Decrease to 0	0

APPENDIX B

THE SIGN OF POLARIZED RADIANCE
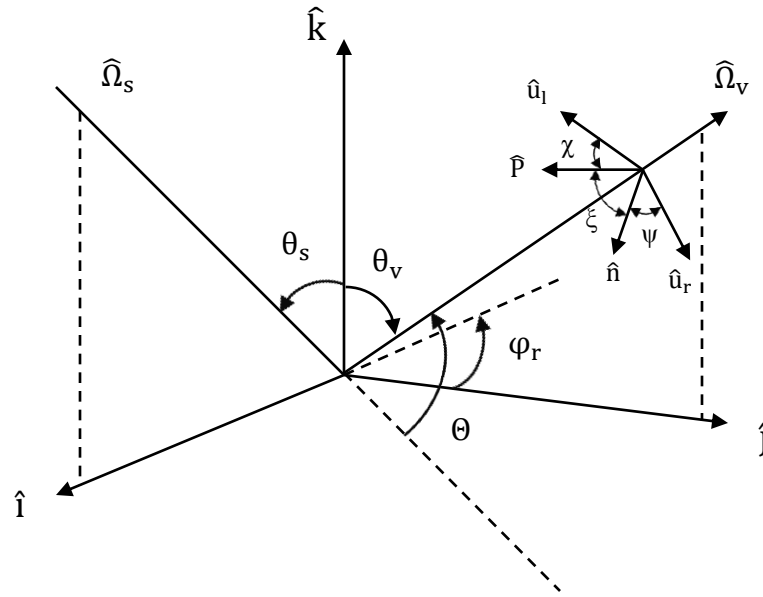
Fig. B.1. POLDER instrument viewing geometry. Adapted from Labonnote et al [49].

This discussion of the sign of polarized radiance follows that of Labonnote [49]. The POLDER instrument on PARASOL measures the polarization in the CCD axes coordinate system $(\hat{u}_r, \hat{u}_l)$ where $\hat{u}_l$ is in the meridian plane as shown in Fig. B1. The direction of polarization χ is just $\frac{1}{2}\arctan(U/Q)$, a result given in Hovenier [36] and many other texts. From Fig. B1 the polarization is then:

$$\hat{P} = \cos\chi\,\hat{u}_l + \sin\chi\,\hat{u}_r . \qquad (65)$$

The $\hat{n}$ direction perpendicular to the scattering plane is given by:

$$\hat{n} = \sin\psi\,\hat{u}_l + \cos\psi\,\hat{u}_r . \qquad (66)$$

Now in the reference frame $(\hat{\imath}, \hat{\jmath}, \hat{k})$ the vectors $\hat{u}_l$, $\hat{u}_r$, and $\hat{n}$ are obtained through the following relations:

$$\hat{u}_r = \begin{pmatrix} \sin \varphi_r \\ \cos \varphi_r \\ 0 \end{pmatrix} \quad \hat{u}_l = \begin{pmatrix} \cos \varphi_r \cos \theta_v \\ -\sin \varphi_r \cos \theta_v \\ \sin \theta_v \end{pmatrix}$$

$$\hat{n} = \begin{pmatrix} \cos \theta_s \sin \theta_v \sin \varphi_r \\ \cos \theta_s \sin \theta_v \cos \varphi_r + \sin \theta_s \cos \theta_v \\ -\sin \theta_s \sin \theta_v \sin \varphi_r \end{pmatrix}. \qquad (67)$$

The angle ψ can be found with the following equations:

$$\sin \psi = -\sin \theta_s \sin \varphi_r$$

$$\cos \psi = \cos \theta_s \sin \theta_v + \sin \theta_s \cos \theta_v \cos \varphi_r. \qquad (68)$$

Now all the equations are written down for the angles needed to obtain the sign. The sign of the polarized radiance is found from the angle ξ, given by:

$$\cos \xi = \hat{n} \cdot \hat{P} = \frac{\sin \psi \cos \chi + \cos \psi \sin \chi}{\sqrt{\sin \psi \sin \psi + \cos \psi \cos \psi}}, \qquad (69)$$

where the denominator of this equation is a normalization factor. If ξ is found to be within the range [45,135] degrees, then the sign of the polarized radiance is negative, whereas outside of this range the sign is positive.

VITA

Benjamin H. Cole received his Bachelor of Science degree in physics from the University of Dallas in May 2009. He continued in the Atmospheric Sciences program at Texas A&M University beginning in September 2009, and received his Master of Science degree in August 2011.

Mr. Cole's research interests are in cloud physics, remote sensing, and the polarization of light. He plans to publish a paper on the topics discussed in this thesis.

Mr. Cole may be contacted at the Department of Atmospheric Sciences, Texas A&M University, 3150 TAMU, College Station, TX 77840-3150. His email address is bcole7347@tamu.edu.